

How dusty is α Centauri?★,★★

Excess or non-excess over the infrared photospheres of main-sequence stars

J. Wiegert¹, R. Liseau¹, P. Thébault², G. Olofsson³, A. Mora⁴, G. Bryden⁵, J. P. Marshall⁶, C. Eiroa⁶, B. Montesinos⁷, D. Ardila^{8,9}, J. C. Augereau¹⁰, A. Bayo Aran^{11,12}, W. C. Danchi¹³, C. del Burgo¹⁴, S. Ertel¹⁰, M. C. W. Fridlund^{15,16}, M. Hajjgholi¹, A. V. Krivov¹⁷, G. L. Pilbratt¹⁸, A. Roberge¹⁹, G. J. White^{20,21}, and S. Wolf²²

(Affiliations can be found after the references)

Received 13 May 2013 / Accepted 21 January 2014

ABSTRACT

Context. Debris discs around main-sequence stars indicate the presence of larger rocky bodies. The components of the nearby, solar-type binary α Centauri have metallicities that are higher than solar, which is thought to promote giant planet formation.

Aims. We aim to determine the level of emission from debris around the stars in the α Cen system. This requires knowledge of their photospheres. Having already detected the temperature minimum, T_{\min} , of α Cen A at far-infrared wavelengths, we here attempt to do the same for the more active companion α Cen B. Using the α Cen stars as templates, we study the possible effects that T_{\min} may have on the detectability of unresolved dust discs around other stars.

Methods. We used *Herschel*-PACS, *Herschel*-SPIRE, and APEX-LABOCA photometry to determine the stellar spectral energy distributions in the far infrared and submillimetre. In addition, we used APEX-SHeFI observations for spectral line mapping to study the complex background around α Cen seen in the photometric images. Models of stellar atmospheres and of particulate discs, based on particle simulations and in conjunction with radiative transfer calculations, were used to estimate the amount of debris around these stars.

Results. For solar-type stars more distant than α Cen, a fractional dust luminosity $f_d \equiv L_{\text{dust}}/L_{\text{star}} \sim 2 \times 10^{-7}$ could account for SEDs that do not exhibit the T_{\min} effect. This is comparable to estimates of f_d for the Edgeworth-Kuiper belt of the solar system. In contrast to the far infrared, slight excesses at the 2.5σ level are observed at $24\ \mu\text{m}$ for both α Cen A and B, which, if interpreted as due to zodiacal-type dust emission, would correspond to $f_d \sim (1-3) \times 10^{-5}$, i.e. some 10^2 times that of the local zodiacal cloud. Assuming simple power-law size distributions of the dust grains, dynamical disc modelling leads to rough mass estimates of the putative Zodi belts around the α Cen stars, viz. $\lesssim 4 \times 10^{-6} M_{\odot}$ of 4 to $1000\ \mu\text{m}$ size grains, distributed according to $n(a) \propto a^{-3.5}$. Similarly, for filled-in T_{\min} emission, corresponding Edgeworth-Kuiper belts could account for $\sim 10^{-3} M_{\odot}$ of dust.

Conclusions. Our far-infrared observations lead to estimates of upper limits to the amount of circumstellar dust around the stars α Cen A and B. Light scattered and/or thermally emitted by exo-Zodi discs will have profound implications for future spectroscopic missions designed to search for biomarkers in the atmospheres of Earth-like planets. The far-infrared spectral energy distribution of α Cen B is marginally consistent with the presence of a minimum temperature region in the upper atmosphere of the star. We also show that an α Cen A-like temperature minimum may result in an erroneous apprehension about the presence of dust around other, more distant stars.

Key words. stars: individual: Alpha Centauri – binaries: general – circumstellar matter – infrared: stars – infrared: planetary systems – submillimeter: stars

1. Introduction

The α Centauri system lies at a distance of only 1.3 pc ($\pi = 747.1 \pm 1.2$ mas, Söderhjelm 1999), with the G2 V star α Cen A (HIP 71683, HD 128620) often considered a solar twin. Together with the K 1 star α Cen B (HIP 71681, HD 128621), these stars are gravitationally bound in a binary system, with an orbital period of close to 80 years and a semi-major axis (24 AU) midway between those of the planets Uranus and Neptune in the solar system. A third star, Proxima Centauri, about 2° southwest of the binary shares a similar proper motion with them and seems currently to be bound to α Cen AB, although the M 6 star α Cen C (HIP 70890) is separated by about 15 000 AU.

* Based on observations with *Herschel* which is an ESA space observatory with science instruments provided by European-led Principal Investigator consortia and with important participation from NASA.

** And also based on observations with APEX, which is a 12 m diameter submillimetre telescope at 5100 m altitude on Llano Chajnantor in Chile. The telescope is operated by Onsala Space Observatory, Max-Planck-Institut für Radioastronomie (MPIfR), and European Southern Observatory (ESO).

The question as to whether there are also planets around our solar-like neighbours has intrigued laymen and scientists alike. The observed higher metallicities in the atmospheres of α Cen A and B could argue in favour of the existence of planets around these stars (Maldonado et al. 2012, and references therein). The proximity of α Cen should allow for highly sensitive observations at high angular resolution with a variety of techniques.

We know today that binarity is not an intrinsic obstacle to planet formation, since more than 12% of all known exoplanets are seen to be associated with multiple systems (Roell et al. 2012). Even if most of these systems have very wide separations (>100 AU) for which binarity might have a limited effect in the vicinity of each star, a handful of planets have been detected in tight binaries of separation ~ 20 AU (e.g., γ Cep, HD 196885), comparable to that of α Cen (Desidera & Barbieri 2007; Roell et al. 2012). The presence of these planets poses a great challenge to the classical core-accretion scenario, which encounters great difficulties in such highly perturbed environments (see review in Thébault 2011).

For the specific case of α Centauri, radial velocity (RV) observations indicate that no planets of mass $>2.5 M_{\text{Jupiter}}$ exist

inside 4 AU of each star (Endl et al. 2001). For their part, theoretical models seem to indicate that in situ planet formation is indeed difficult in vast regions around each star, because the outer limit for planet accretion around either star is ~ 0.5 – 0.75 AU in the most pessimistic studies (Thébaud et al. 2009) and ~ 1 – 1.5 AU in the most optimistic ones (e.g. Xie et al. 2010; Paardekooper & Leinhardt 2010). However, these estimates open up the possibility that planet formation should be possible in the habitable zone (HZ) of α Cen B, which extends between 0.5 and 0.9 AU from the star (Guedes et al. 2008). Very recently, based on a substantial body of RV data, Dumusque et al. (2012) have proposed that an Earth-mass planet orbits α Cen B with a three-day period (but see Hatzes 2013). In other words, the radial distance of α Cen Bb (0.04 AU), which corresponds to only nine stellar radii, is evidently far inside the HZ, and therefore the surface conditions should be far from able to support any form of life as we know it.

Based on sensitive *Herschel* (Pilbratt et al. 2010) observations, a relatively large fraction of stars with known planets exhibit detectable far-infrared (FIR) excess emission due to cool circumstellar dust (Eiroa et al. 2011; Marshall et al. 2014; Krivov et al. 2013), akin to the debris found in the asteroid (2–3 AU) and Edgeworth-Kuiper (30–55 AU) belts of the solar system. As part of the *Herschel* open time key programme DUNES around NEarby Stars (DUNES; Eiroa et al. 2013), we observed α Cen to search for dust emission associated with the stars, which is thought to develop on planetesimal size scales and to be ground down to detectable grain sizes by mutual collisions. Persistent debris around the stars would be in discs of a few AU in size and would re-emit intercepted starlight in the near- to mid-infrared. To within 16%, ISO-SWS observations did not detect any excess above the photosphere of α Cen A between 2.4 and 12 μm (Decin et al. 2003, and Fig. 7 below). On the other hand, a circumbinary Edgeworth-Kuiper belt analogue would be much larger and the dust much cooler, so that it would emit predominantly at FIR and submillimetre (submm) wavelengths. Such a belt would be spatially resolved with the *Herschel* beam, in principle allowing the detection of structures due to dynamical interactions with, say, a binary companion and/or giant planets (e.g. Wyatt 2008, and references therein), but its surface brightness could be expected to be very low, rendering such observations very difficult.

The DUNES programme focusses on nearby solar-type stars, and the observations with *Herschel*-PACS (Poglitsch et al. 2010) at 100 μm and 160 μm are aimed at detecting the stellar photospheres at an $S/N \geq 5$ at 100 μm and has observed 133 nearby Sun-like stars (FGK type, $d < 25$ pc). Prior to *Herschel*, little data at long wavelengths that have high photometric quality are available for α Cen A and B. One reason for this is probably detector saturation issues due to their brightness (e.g. WISE bands W1–W4), and another is due to contamination in the large beams by confusing emission near the galactic plane (e.g. IRAS, ISO-PHOT, and AKARI data).

Due to their proximity and with an age comparable to that of the Sun (4.85 Gyr, Thévenin et al. 2002), α Cen is an excellent astrophysical laboratory for “normal” low-mass stars, otherwise known to be very difficult to calibrate, not the least with respect to their ages. From numerous literature sources, Torres et al. (2010) have compiled the currently best available basic stellar parameters of the α Cen system. The given errors on the physical quantities are generally small. However, whereas the tabulated uncertainty of the effective temperature of e.g. α Cen A is less than half a percent, the observed spread in Table 1 of Porto de Mello et al. (2008) corresponds to more than ten times

this much. On the other hand, the radii given by Torres et al. (2010) are those directly measured by Kervella et al. (2003) using interferometry, with errors of 0.2% and 0.5% for A and B, respectively (Bigot et al. 2006). Masses have been obtained from astroseismology and are good to within 0.6% for both components (Thévenin et al. 2002).

For such an impressive record of accuracy for the stellar parameters of the α Cen components, it should be possible to construct theoretical model photospheres with which observations can be directly compared to a high level of precision. Here, we report PACS observations of α Cen at 100 μm and 160 μm . These single-epoch data are complemented by LABOCA (Siringo et al. 2009) data at 870 μm obtained during two different epochs. The LABOCA observations primarily address two issues: the large proper motion ($3''.7 \text{ yr}^{-1}$) should enable the discrimination against background confusion and, together with SPIRE photometry (see below), these submm data should also provide valuable constraints on the spectral energy distributions (SEDs). This could potentially be useful for quantifying some of the properties of the emitting dust and/or to gauge the temperature minima at the base of the stellar chromospheres. A clear understanding of the latter is crucial when attempting to determine extremely low levels of cool circumstellar dust emission.

The paper is organised as follows. Section 2 outlines our observations with various facilities, both from space and the ground. Since we are aiming at low-level detections, the reduction of these data is described in detail. Our primary results are communicated in Sect. 3. In the discussion Sect. 4, we examine the lower chromospheres of the α Cen stars in terms of the radiation temperatures from their FIR photospheres. Possible contributions to the FIR/submm SEDs by dust are also addressed, using both analytical estimations and detailed numerical models. Finally, Sect. 5 provides a quick overview of our conclusions.

2. Observations and data reduction

2.1. *Herschel*

In the framework of our observing programme, i.e. the DUNES open time key programme, PACS photometric images were obtained at 100 μm and 160 μm . In addition, from the Hi-GAL survey (PI S. Molinari), we acquired archive data for α Cen at 70 μm and 160 μm obtained with PACS and at 250 μm , 350 μm , and 500 μm with SPIRE (Griffin et al. 2010). The relative position of the stars in the sky during the observational period is shown in Fig. 1.

2.1.1. DUNES: PACS 100 μm and 160 μm

PACS scan maps of α Cen were obtained at 100 μm and 160 μm at two array orientations (70° and 110°) to suppress detector striping. The selected scan speed was the intermediate setting, i.e. $20'' \text{ s}^{-1}$, determining the PSF at the two wavelengths ($7''.7$ and $12''$, respectively). The 100 μm filter spans the region 85–130 μm and the 160 μm filter 130–210 μm and the observations at 100 and 160 μm were made simultaneously. The data were reduced with HIPE v.8.0.1. The native pixel sizes are $3''.2$ and $6''.4$ at 100 and 160 μm , respectively, and in the reduced images the resampling resulted in square pixels of $1''$ at 100 μm and $2''$ at 160 μm .

The two stellar components are approximated by model instrument PSFs of the appropriate wavelength based on an observation of α Boo rotated to match the telescope position angle of the α Cen observations. It is important to match the

Table 1. Observing log.

Instrument/ mode	Obs/Pgm ID	Wavelength λ_{eff} (μm)	Beam width HPBW ($''$)	Observing date year–mo–day	t_{int} (s)	Centre coordinates ^a h m s ° ' "	Offset ^b ($''$)
<i>Herschel</i> -PACS	1342224848	100	7 $''$.7	2011–07–29	542	14 39 30.200 –60 49 59.66	1.7
	1342224849	160	11 $''$.3	2011–07–29	542	14 39 30.115 –60 49 59.54	1.3
SpirePacsParallel	1342203280	70	5 $''$.9 \times 12 $''$.2	2010–08–21	9490	14 28 59.831 –60 39 01.60	2 $^\circ$ \times 2 $^\circ$ map
	1342203281	160	11 $''$.6 \times 15 $''$.6	2010–08–21
	...	250	17 $''$.6 ^c	2010–08–21
	...	350	23 $''$.9 ^c	2010–08–21
	...	500	35 $''$.2 ^c	2010–08–21
APEX-LABOCA	384.C-1025(A)	870	19 $''$.5	2009–09–19	7147	14 39 31.725 –60 49 59.10	3.7
	380.C-3044(A)	870	19 $''$.5	2007–11–10 to 13	34 026	14 39 32.349 –60 50 00.00	3.6
APEX-SHeFI	090.F-9322(A)	1300	27 $''$.1	2012–08–16	2646	14 39 35.060 –60 50 15.1	sp. line map

Notes. ^(a) Observed equatorial coordinates (J2000) towards the target, i.e. the centre of the fitted point source, which refers to the primary α Cen A, except for Hi-GAL and APEX-SHeFI maps. ^(b) Offset of observed with respect to intended (= commanded) position. Except for SHeFI, coordinates are corrected for the stellar proper and orbital motions. Not applicable (na) to survey data. ^(c) According to the SPIRE manual, see <http://herschel.esac.esa.int/Docs/SPIRE/html/>, the average beam area is 423 arcsec² at 250 μm , 751 arcsec² at 350 μm and 1587 arcsec² at 500 μm .

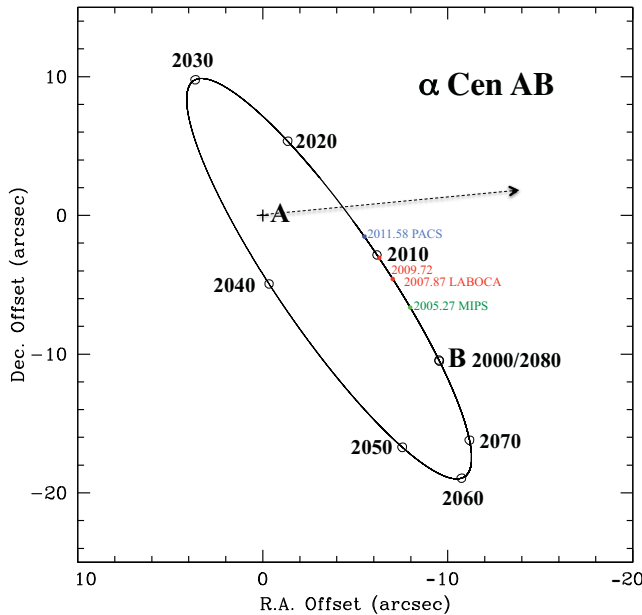


Fig. 1. Binary α Cen AB as it appears in the sky on various occasions. Shown is the orbit of α Cen B with respect to the primary A, which is at the origin, and with north up and east to the left. During the observing period, the separation of the stars was greatest in 2005 and smallest in 2011. The relative positions in the PACS (blue) and LABOCA (red) maps are indicated. The proper motion of α Cen for the time span between the LABOCA and PACS observations is shown by the dashed arrow. The separation between the stars at the time of the MIPS observations is indicated by the green dot. Orbital elements are adopted from Pourbaix et al. (2002).

orientation of the PSF due to the non-circular tri-lobal structure of the *Herschel*-PACS PSF, which exists below the 10% peak flux level.

Fitting of the two components was carried out by subtracting the components in series, starting with the brighter one. Each component model PSF was scaled to the estimated peak brightness and shifted to the required positional offset from the observed source peak before subtraction. The position offset of B relative to A was fixed.

As described in detail by Eiroa et al. (2013), the level of the background and the rms sky noise were estimated by calculating the mean and standard deviation of 25 boxes sized 9 $''$ \times 9 $''$ at 100 μm and 14 $''$ \times 14 $''$ at 160 μm scattered randomly at positions lying between 30 $''$ –60 $''$ from the image centre and within the area of which no pixel was brighter than twice the standard deviation of all non-zero pixels in the image (the threshold criterion for source/non-source determination while high pass filtering during map creation). The calibration uncertainty was assumed to be 5% for both 100 μm and 160 μm (Balog et al. 2013)¹.

Aperture (and potential colour) corrections of the stellar flux densities and sky noise corrections for correlated noise in the super-sampled images are described in the technical notes PICC-ME-TN-037 and PICC-ME-TN-038 and the NHSC/PACS home page².

2.1.2. Hi-GAL: PACS 70 μm and 160 μm

As part of the Hi-GAL program, these data were obtained at a different scan speeds, i.e. the fast mode at 60 $''$ s⁻¹. The field 314_0, containing α Centauri, was observed at both wavelengths simultaneously and in parallel with the SPIRE instrument (see next section). The scanned area subtends 2 $^\circ$ \times 2 $^\circ$ and these archive data are reduced to Level 2.5. Compared to the data at longer wavelengths, background problems are much less severe at 70 μm . The PACS 70 μm data provide the highest angular resolution of all data presented here (Table 1). As before, no further colour correction was required, but the proper aperture correction (1.22) was applied. After re-binning, the pixel size is the same as that at 100 μm , viz. one square arcsecond, whereas the 160 μm pixels are, as before, two arcseconds squared.

2.1.3. Hi-GAL: SPIRE 250 μm , 350 μm , and 500 μm

At the relatively low resolution of the SPIRE observations, the strong and varying background close to α Cen presented a considerable challenge for the flux measurements. However, for

¹ The PACS calibration scheme is described further in detail at http://herschel.esac.esa.int/twiki/bin/view/Public/PacsCalibrationWeb#PACS_instrument_and_calibration

² <https://nhscsci.ipac.caltech.edu/sc/index.php/Pacs/AbsoluteCalibration>

Table 2. Photometry and FIR/flux densities of α Centauri.

λ_{eff} (μm)	α Cen A S_{ν} (Jy)	α Cen B S_{ν} (Jy)	Photometry & reference
0.440	2215 \pm 41	536 \pm 10	<i>B</i> (1)
0.550	3640 \pm 67	1050 \pm 19	<i>V</i> (1)
0.790	4814 \pm 89	1654 \pm 30	<i>I</i> (1)
0.440	2356 \pm 43	572 \pm 10	<i>B</i> (2)
0.550	3606 \pm 66	1059 \pm 20	<i>V</i> (2)
0.640	4259 \pm 78	1387 \pm 26	<i>R_c</i> (2)
0.790	4784 \pm 88	1666 \pm 31	<i>I_c</i> (2)
1.215	4658 \pm 86	1645 \pm 30	<i>J</i> (3)
1.654	3744 \pm 69	1649 \pm 31	<i>H</i> (3)
2.179	2561 \pm 47	1139 \pm 21	<i>K</i> (3)
3.547	1194 \pm 22	521 \pm 10	<i>L</i> (3)
4.769	592 \pm 11	258 \pm 5	<i>M</i> (3)
24	30.84 \pm 0.76	13.63 \pm 0.33	MIPS (4)
70	3.35 \pm 0.28	1.49 \pm 0.28	PACS (5)
100	1.41 \pm 0.05	0.67 \pm 0.037	PACS (6)
160	0.56 \pm 0.06	0.21 \pm 0.06	* PACS (5), (6)
250	0.24 \pm 0.05	0.11 \pm 0.05	* SPIRE (5)
350	0.145 \pm 0.028	0.064 \pm 0.028	* SPIRE (5)
500	0.08 \pm 0.03	0.04 \pm 0.03	* SPIRE (5)
870	0.028 \pm 0.007	0.012 \pm 0.007	* LABOCA (7)

Notes. ^(*) Asterisks indicate values determined using $S_{\nu,A}/S_{\nu,B} = 2.25$ (see Liseau et al. 2013).

References. (1) HIPPARCOS. (2) Bessell (1990). (3) Engels et al. (1981). (4) A. Mora (priv. comm.; $\text{FWHM}(24\mu\text{m}) = 6''$). Binary separation on 9 April 2005, $10''4$ (5) Hi-GAL: KPOT_smolinar_1, fields 314_0 & 316_0. *Herschel*-beams $\text{FWHM}(70\mu\text{m}) = 5''6$, $(100\mu\text{m}) = 6''8$, $(160\mu\text{m}) = 11''3$, $(250\mu\text{m}) = 17''6$, $(350\mu\text{m}) = 23''9$, $(500\mu\text{m}) = 35''2$. Binary separation on 21 August 2010, $6''3$. (6) DUNES: KPOT_ceiroa_1. Binary separation 29 July 2011, $5''7$. (7) 384.C-1025, 380.C-3044(A): $\text{FWHM}(870\mu\text{m}) = 19''5$. Binary separation 20–13 November 2007, $8''8$ and 19 September 2009, $7''0$.

wavelengths beyond $160\mu\text{m}$, the dust emission from the galactic background is expected to be in the Rayleigh-Jeans (RJ) regime, and the emissivity should remain reasonably constant. Therefore, when normalised to a specific feature, the background is expected to look essentially the same at all wavelengths, when disregarding the slight deterioration of the resolution due to the smearing at the longest wavelengths. The result of this procedure is shown in Fig. 4, where α Cen is represented by the scaled PSFs and the background-subtracted fluxes are reported in Table 2. Assuming 10–30% higher (lower) fluxes for α Cen results in depressions (excesses) at the stellar position, which are judged unrealistic. This should therefore provide a reasonable estimate of the accuracy of these measurements. The photometric calibration of SPIRE is described by Bendo et al. (2013).

2.2. APEX

The Atacama Pathfinder EXperiment (APEX) is a 12 m submillimetre (submm) telescope located at 5105 m altitude on the Llano de Chajnantor in Chile. According to the APEX home page³, the telescope pointing accuracy is $2''$ (rms). The general user facilities include four heterodyne receivers within the approximate frequency bands 200–1400 GHz and two bolometer arrays, centred at 345 GHz ($870\mu\text{m}$) and 850 GHz ($350\mu\text{m}$),

³ <http://www.apex-telescope.org/telescope/>

respectively. We used LABOCA and SHeFI APEX-1 for the observations of α Centauri.

2.2.1. LABOCA $870\mu\text{m}$

The Large APEX Bolometer Camera (LABOCA) is a submillimetre array mounted on the APEX telescope (Siringo et al. 2009). The operating wavelength is $870\mu\text{m}$ centred on a $150\mu\text{m}$ wide window (345 and 60 GHz, respectively). With separations of $36''$, the 295 bolometers yield a circular field of view of $11'4$. The angular resolution is $\text{HPBW} = 19''5$ and the under-sampled array is filled during the observations with a spiral mapping method.

The mapping observations of α Cen were made during two runs, viz. on 10–13 November 2007, and on 19 September 2009. The data associated with the programmes 380.C-3044(A) and 384.C-1025(A) were retrieved from the ESO archive. Since this observing mode is rather inefficient for point sources, we performed additional test observations with the newly installed telescope wobbler on 20 May and 13–14 July 2011. While centring α Cen B on LABOCA channel 71, the chopping was done by a fixed $\pm 25''$ in east-west direction, which resulted in asymmetric sky-flux pickup in this confused field, and these data therefore had to be discarded.

The map data were reduced and calibrated using the software package CRUSH 2 developed by Attila Kovács⁴. The data have been smoothed with a Gaussian of $\text{HPBW} = 13''$, resulting in an effective $\text{FWHM} = 23''4$. However, fluxes in Jy/beam are given for an $\text{FWHM} = 19''5$.

2.2.2. SHeFI 230 GHz ($1300\mu\text{m}$)

Complementing observations were made with the Swedish Heterodyne Facility Instrument (SHeFI) APEX-1 during Director’s Discretionary Time (DDT) on 16 August 2012. APEX-1 is a single-sideband receiver that operates in the 230 GHz band (211–275 GHz) with an IF range of 4–8 GHz. At the CO (2–1) frequency, 230.5380 GHz, the half-power-beamwidth is $27''$. The estimated main beam efficiency is $\eta_{\text{mb}} = 0.75$, and the kelvin-to-jansky conversion for the antenna is 39 Jy/K at this frequency.

The observing mode was on-the-fly (OTF) mapping with a scan speed of $6''\text{s}^{-1}$, which resulted in a data cube for the $5' \times 5'$ spectral line map with 441 read-out points (Fig. 6). The reference, assumed free of CO emission, was at offset position ($+1500''$, $-7200''$). During the observations, the system noise temperature was typically $T_{\text{sys}} = 200$ K. As backend we used the fast Fourier transform spectrometer (FFTS) configured to 8192 channels having velocity resolution 0.16 km s^{-1} , yielding a total Doppler bandwidth of 1300 km s^{-1} .

These ON-OFF observations generate a data cube with two spatial dimensions (the “map”) and one spectral dimension (intensity vs frequency spectrum). The data were reduced with the xs-package by P. Bergman⁵. This included standard, low order, base line fitting, and subtraction, yielding for each “pixel” a spectrum with the intensity given relative to the zero-kelvin level (see Fig. 6a).

⁴ See: <http://www.submm.caltech.edu/~sharc/crush/download.htm>

⁵ <http://www.chalmers.se/rss/oso-en/observations/data-reduction-software>

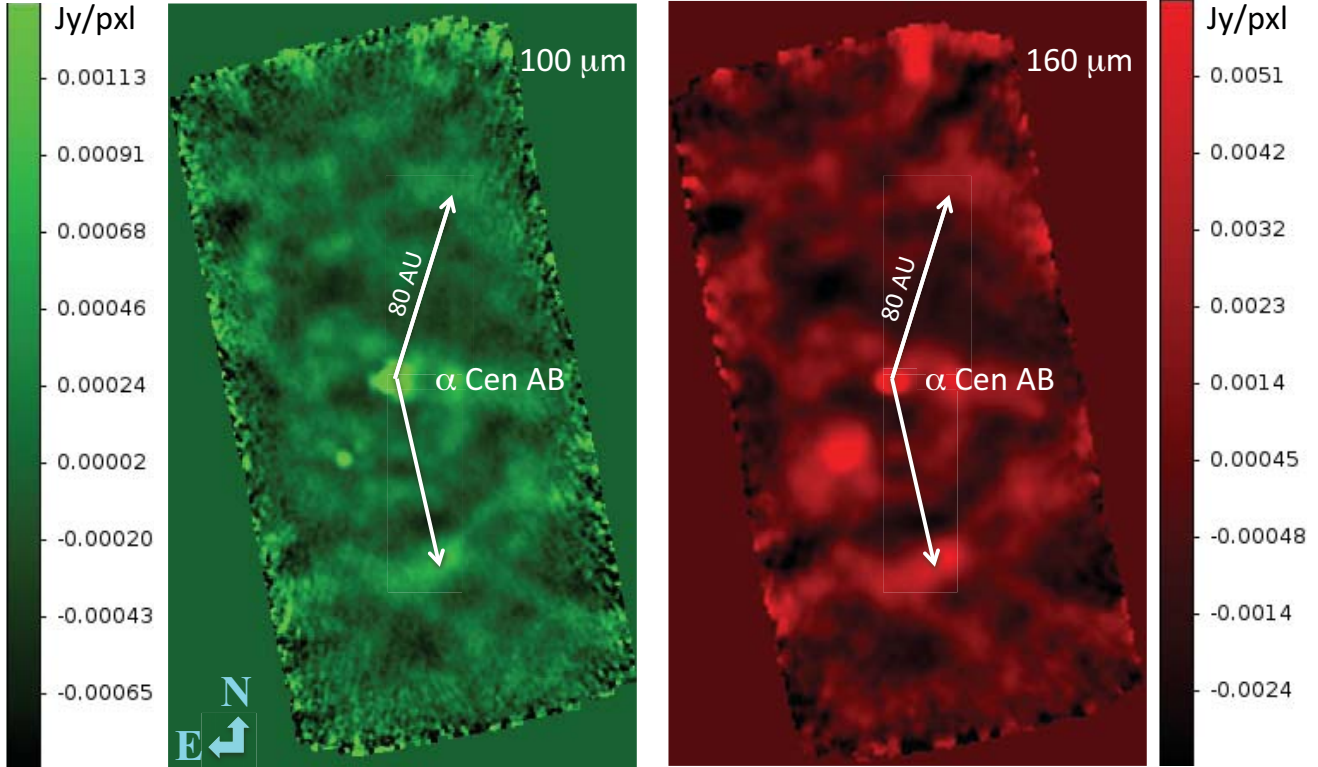


Fig. 2. Binary α Cen at $100\mu\text{m}$ (left: green) and $160\mu\text{m}$ (right: red) at high contrast. Scales are in Jy/pxl, where square pixels are $1''$ on a side at $100\mu\text{m}$ and $2''$ on a side at $160\mu\text{m}$. The field of view is 1.75×3.5 . The image of α Cen is extended in the direction of the companion and, at $100\mu\text{m}$, the pair is quasi-resolved, having a separation of 5.7 along position angle 254° . The white arrows of length 80 AU correspond approximately to the stable circumbinary regime around α Cen AB. These point to parts of coherent structures that are also seen at all FIR/submm wavelengths.

3. Results

3.1. Herschel PACS and SPIRE

The stars were clearly detected at both PACS $100\mu\text{m}$ and $160\mu\text{m}$, as expected on the basis of the adopted observing philosophy of the DUNES programme. The last entry in Table 1 refers to the difference between the commanded position, corrected for proper and orbital motion, and the observed position, determined from the fitting of Gaussians to the data, and these are found to clearly be less than $2''$. This compares very favourably with the findings for PACS of the average offset of $2.4''$ by Eiroa et al. (2013) for a sample of more than 100 solar type stars. Similarly, observed offsets are also acceptable for the LABOCA data, i.e. within 2σ of the claimed pointing accuracy (Table 1).

Observed flux densities of α Cen A and B are given in Table 2, where the quoted errors are statistical and only refer to relative measurement accuracy. Absolute calibration uncertainties are provided by the respective instrument teams and cited here in the text. Together with complementing *Spitzer* MIPS data, these data are displayed in Fig. 7. For both α Cen A and B, a marginal excess at $24\mu\text{m}$ corresponding to 2.5σ and 2.6σ is determined, respectively. The measured flux ratio at this wavelength corresponds well with the model ratio, i.e. 2.26 ± 0.11 and 2.25 respectively.

α Cen was detected at all SPIRE wavelengths, but with a marginal result at $500\mu\text{m}$ (Fig. 5 and Table 2). As is also evident from these images, the pair was not resolved.

3.2. APEX LABOCA

The LABOCA fields are significantly larger than those of the PACS frames, and they contain a number of mostly extended sources of low intensity. However, α Cen is clearly detected (Fig. 5), but the binary components are not resolved. In Table 2, only the average is given for the 2007 and 2009 observations, because these flux densities are the same within the errors.

The proximity of the α Cen system leads to angular size scales that are rarely ever encountered among debris discs, which are generally much farther away. The PACS field of view is $105'' \times 210''$, so that a Edgeworth-Kuiper belt analogue would easily fill the images. The LABOCA frames contain structures similar to those discernable in Fig. 2. Although at faint levels, most of these sources are definitely real, because they repeatedly show up in independent data sets at different wavelengths obtained with different instruments and at different times. Knotty, but seemingly coherent, arcs and ring-like features on arcmin scales mimic the morphology of belt features. If these features were associated with the α Cen stars, they should move in concert with them at relatively high speeds. At $870\mu\text{m}$, the strongest feature lies less than one arcminute southeast of α Cen and is barely detectable at $100\mu\text{m}$, but clearly revealed at $160\mu\text{m}$. Measurements of the sky positions for both this feature (“Bright Spot”) and α Cen are reported in Table 3. For the Bright Spot these differ by $+1.2$ in right ascension (RA) and $+0.9$ in declination (Dec.), which provides an estimate of the measurement error, i.e. $\sim 1''$ for relatively bright and centrally condensed sources.

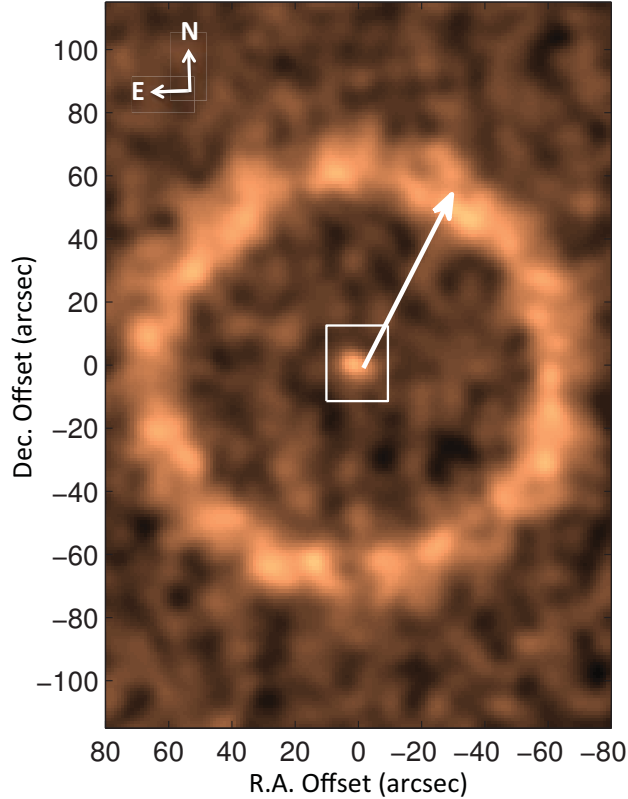


Fig. 3. Simulated observation at $160\ \mu\text{m}$ of α Cen AB, assuming a face-on circumbinary dust disc/ring ($m_d \sim 0.1 M_\odot$, cf. Sect. 4.5.2). As seen from the system’s barycentre (white rectangle), the ring extends from 70 to 105 AU. (The white arrow has a length of 80 AU.) In this image, each pixel is $1''.04$ on a side. The image was smoothed with a 16×16 pixel Gaussian filter with a standard deviation of 3 pixels. The added noise is also Gaussian-distributed and smoothed to mimic the noise and beam size of Fig. 2.

Table 3. Dual epoch position data with LABOCA.

Object	Year	RA (J2000)	Dec (J2000)
α Centauri AB	2007	14 39 32.174	−60 50 02.5
	2009	14 39 31.246	−60 49 59.6
Bright Spot	2007	14 39 33.953	−60 50 44.5
	2009	14 39 34.120	−60 50 43.6

Owing to its high proper motion, these values are significantly higher for α Cen, viz. $\Delta \text{RA} = -6''.8$ and $\Delta \text{Dec} = +2''.9$, at position angle $\text{PA} \sim 247^\circ$. Neglecting the $0''.1$ parallactic contribution, SIMBAD⁶ data for α Cen yield for the 1.856 yr observing period $\Delta \text{RA} = -6''.7$, $\Delta \text{Dec} = +1''.3$, and $\text{PA} = 259^\circ$.

Similar results are obtained involving other features in the $870\ \mu\text{m}$ images. This provides firm evidence that the inhomogeneous background is stationary and an unlikely part of any circumbinary material around α Cen AB. A few notes concerning the nature of this background are given in the next section.

⁶ <http://simbad.u-strasbg.fr/simbad/>

3.3. APEX-1 SHeFI

In the direction of α Cen, strong CO(2–1) emission lines are found at local-standard-of-rest (LSR) velocities of -30 , -50 , and $-60\ \text{km s}^{-1}$, with a weaker component also at $+40\ \text{km s}^{-1}$. This is entirely in accord with the observations of the Milky Way in CO(1–0) by Dame et al. (2001). As an example, the distribution of the integrated line intensity of the $-50\ \text{km s}^{-1}$ component is shown in Fig. 6, providing an overview of the molecular background in this part of the sky. With the line widths typical of giant molecular clouds, this confusing emission is certainly galactic in origin and not due to an anonymous IR-galaxy because the lines would be too narrow. We can also exclude the possibility of a hypothetical circumbinary dust disc around the pair α Cen AB, since the observed lines fall at unexpected LSR-velocities ($v_{\alpha \text{ Cen}} \sim -3\ \text{km s}^{-1}$) and are also too wide and too strong. Since these data do not reveal the continuum, the stars α Cen AB are not seen in the CO line maps.

4. Discussion

4.1. FIR and submm backgrounds

At a distance of 1.3 pc and located far below the ecliptic plane, any foreground confusion can be safely excluded. At greater distances, bright cirrus, dust emission from galactic molecular clouds, PDRs, H II regions, and/or background galaxies potentially contribute to source confusion at FIR and submm wavelengths. However, the projection of α Cen close to the galactic plane makes background issues rather tricky (see Sect. 2.1.3). In particular, extragalactic observers tend to avoid these regions, and reliable catalogues for IR galaxies are generally not available. However, as our spectral line maps show (Fig. 6), the observed patchy FIR/submm background is clearly dominated by galactic emission.

4.2. The SEDs of α Cen A and α Cen B

4.2.1. The stellar models

For the interpretation of the observational data we need to exploit reliable stellar atmosphere models and stellar physical parameters. The model photosphere parameters are based on the weighted average as the result of an extensive literature survey. The models have been computed by a 3D interpolation in a smoothed version of the high-resolution PHOENIX/GAIA grid (Brott & Hauschildt 2005) and with the following parameters from Torres et al. (2010) and the metallicities from Thévenin et al. (2002): $(T_{\text{eff}}, \log g, [\text{Fe}/\text{H}]) = (5824\ \text{K}, 4.3059, +0.195)$ for α Cen A and $(5223\ \text{K}, 4.5364, +0.231)$ for α Cen B. These models are shown in Fig. 7, together with the photometry (Table 2). We wish to point out again that these data have not been used in the analysis, but merely serve to illustrate the goodness of the models.

As a sanity check we compared the integrated model fluxes with the definition of the effective temperature, $\int S_\nu d\nu / \int B_\nu(T_{\text{eff}}) d\nu$. The luminosities are conserved to within 0.6% for α Cen A and 0.1% for α Cen B, which is well within the observational errors of 2% and 5%, respectively (Torres et al. 2010), which in turn are comparable to the errors of the theoretical model (e.g. Gustafsson et al. 2008; Edvardsson 2008). These small differences can probably be traced back to the re-gridding of the high-resolution models onto a somewhat sparser spectral grid.

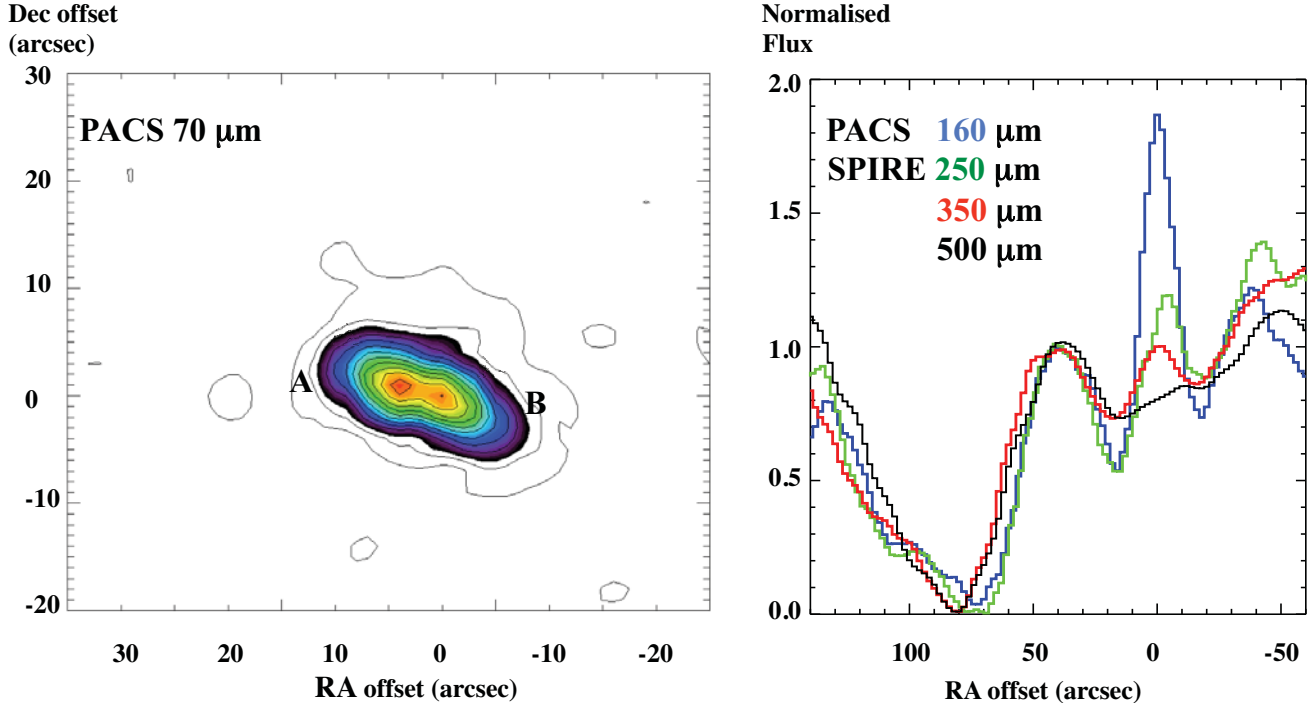


Fig. 4. *Left:* at $70\ \mu\text{m}$ with PACS, the binary α Cen AB is clearly resolved (Hi-GAL data). As a result of the re-binning using cubic spline interpolation, the stars appear too close in this image. *Right:* the method for the estimation of the source and background fluxes in the SPIRE images is illustrated. Shown is a cut in right ascension through the image, normalised to the interstellar dust feature $40''$ east of α Cen. For comparison, the $160\ \mu\text{m}$ PACS data are also shown in blue. For SPIRE, green identifies $250\ \mu\text{m}$, red $350\ \mu\text{m}$, and black $500\ \mu\text{m}$.

4.2.2. The temperature minima of α Cen A and α Cen B

At heights of some five hundred kilometers above the visible photosphere ($h \lesssim 10^{-3} R_{\odot}$), the Sun exhibits a temperature minimum, i.e. $T/T_{\text{eff}} < 1$, beyond which temperatures rise into the chromosphere and corona. Theories attempting to explain the physics of the heating of these outer atmospheric layers generally invoke magnetic fields (Carlsson & Stein 1995), but the details are far from understood and constitute an active field of solar research (e.g. de la Cruz Rodríguez et al. 2013). Such atmospheric structure can be expected to also be quite common on other and, in particular, solar-type stars. There, the dominating opacity, viz. H^- free-free, limits the visibility to the FIR photosphere. For instance, on the Sun, T_{min} occurs at wavelengths around $150\ \mu\text{m}$. This is very close to the spectral region, where this phenomenon has recently been directly measured for the first time also on another star (viz. α Cen A, Liseau et al. 2013), where in contrast to the Sun, the spatial averaging over the unresolved stellar disc is made directly by the observations. Since it is so similar in character, α Cen A may serve as a proxy for the Sun as a star (see also Pagano et al. 2004).

This T_{min} -effect has also been statistically observed for a larger sample of solar-type stars (see Fig. 6 of Eiroa et al. 2013), a fact that could potentially contribute to enhancing the relationship between solar physics and the physics of other stars. In the end, such observations may help to resolve a long-standing puzzle in solar physics concerning the very existence of an actual gas temperature inversion at 500 km height and concerning whether this is occurring in the Quiet Sun or in active regions on the Sun (e.g., Leenaarts et al. 2011; Beck et al. 2013). Theoretical models have hitherto been inconclusive.

For α Cen A, Liseau et al. (2013) find that $T_{\text{min}} = 3920 \pm 375\ \text{K}$, corresponding to the ratio $T_{\text{min}}/T_{\text{eff}} = 0.67 \pm 0.06$. This

is lower than observed for the Sun from spectral lines in the optical, viz. ~ 0.78 from analysis of the Ca II K-line (Ayres et al. 1976). These authors also estimated this ratio for α Cen B, i.e. 0.71 and 0.72 using $T_{\text{eff}} = 5300$ and $5150\ \text{K}$, respectively. For the data displayed in Fig. 7, we arrive at an estimate of $T_{\text{min}} = 3020 \pm 850\ \text{K}$ near $160\ \mu\text{m}$ for this star. This results in $T_{\text{min}}/T_{\text{eff}} = 0.58 \pm 0.17$, with $T_{\text{eff}} = 5223 \pm 62\ \text{K}$. This value for α Cen B is slightly lower than the optically derived value, but the error on the infrared ratio is large. However, also for the Sun itself, T_{min} determinations at different wavelengths show a wide spread of several hundred Kelvin (Avrett 2003).

In the present paper, we are however primarily concerned with the possible effects T_{min} might have on estimation of very low emission levels from exo-Edgeworth-Kuiper belt dust. The intensity of the stellar model photosphere beyond 20 to $40\ \mu\text{m}$ is commonly estimated from the extrapolation of the SED into the Rayleigh-Jeans (RJ) regime at the effective temperature T_{eff} . There is a potential risk that this procedure will overestimate actual local stellar emissions, which may be suppressed at the lower radiation temperatures. In those cases where the SEDs are seemingly well fit by the RJ-extrapolations, the differences may in fact be due to emission from cold circumstellar dust (exo-Edgeworth-Kuiper belts), and here, we wish to quantify the magnitude of such an effect.

4.3. Far infrared: detectability of cool dust from Edgeworth-Kuiper belt analogues

The SED of α Cen A is exceptionally well-determined over a broad range of wavelengths, and we use it here for the estimation of the likely level of this effect on other, non-resolved systems. We do that by “filling the pit with sand” to determine the

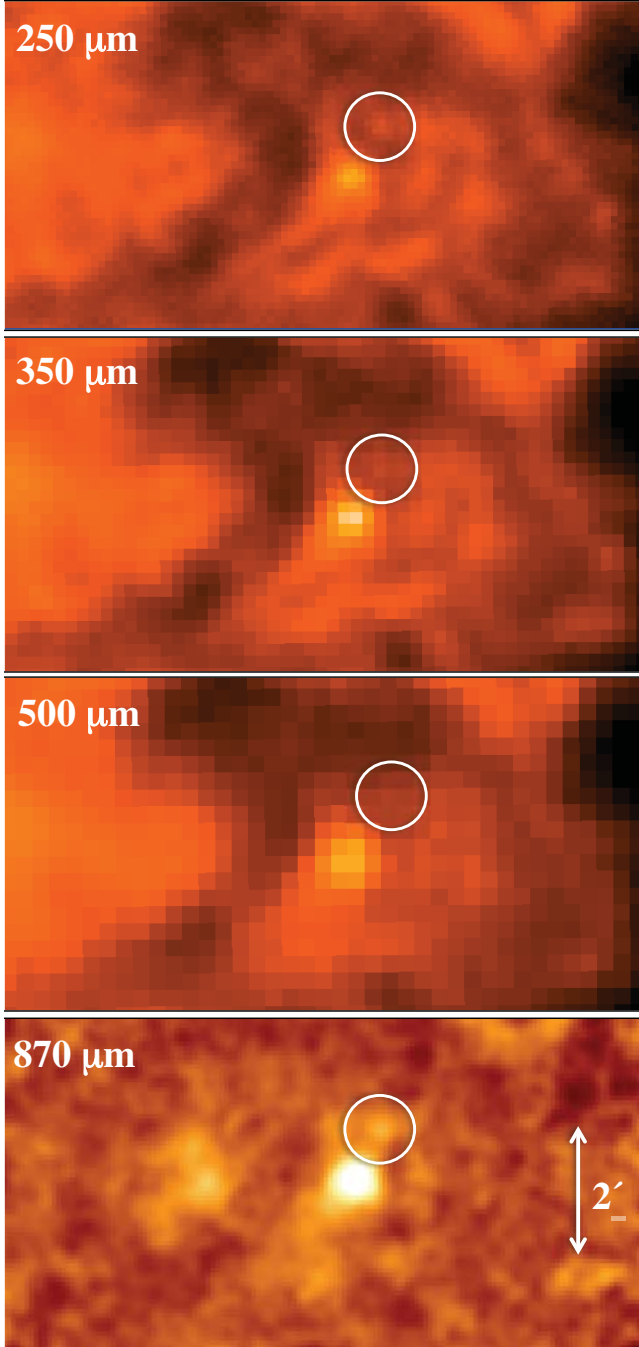


Fig. 5. Gallery of SPIRE and LABOCA data for α Centauri, which is inside the circles. *Top to bottom:* 250 μm , 350 μm , and 500 μm (SPIRE) and 870 μm (LABOCA), where the length of the arrow corresponds to 2'.

corresponding fractional dust luminosity $f_d \equiv L_{\text{dust}}/L_{\text{star}}$ and the accompanying temperature of the hypothetical dust.

True Edgeworth-Kuiper belt analogues would be extremely faint and very difficult to detect ($f_{d\odot} \sim 10^{-7}$; Teplitz et al. 1999; Shannon & Wu 2011; Vitense et al. 2012). For estimating faint exo-Edgeworth-Kuiper belt levels, we apply simple dust ring models to “fill” the flux-dip of the temperature minimum of α Cen A, i.e. by minimising the chi-square for

$$\chi_\nu = \frac{S_{\text{dust}}(\nu) - S_{\text{model}}(\nu)}{\sigma}, \quad \text{with limiting } \chi^2 \leq 10^{-4}. \quad (1)$$

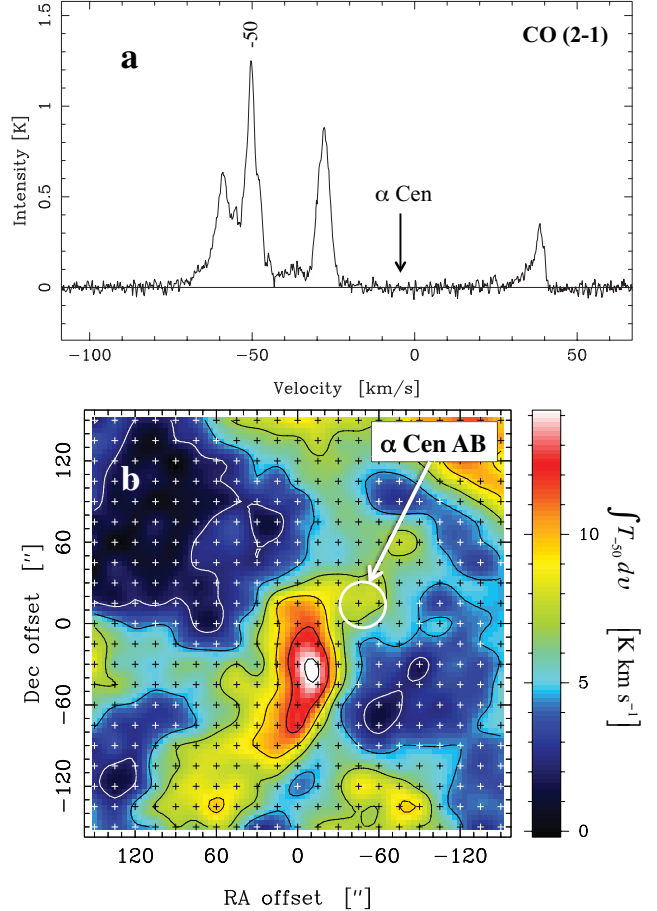


Fig. 6. **a)** Grand average of all CO(2–1) spectra, in T_{mb} vs. v_{LSR} , of the $5' \times 5'$ map toward α Centauri. Strong emission features at several lsr-velocities are evident in this direction of the Galaxy ($\ell^{\text{II}} = 315^\circ 73$, $b^{\text{II}} = -0^\circ 68$), with the strongest line at $v_{\text{LSR}} = -50 \text{ km s}^{-1}$. **b)** Integrated intensity map of the CO(2–1) line at $v_{\text{LSR}} = -50 \text{ km s}^{-1}$, i.e. $\int T_{-50} dv$, in the direction of α Centauri (for APEX and at $\nu = 230 \text{ GHz}$, $\int T dv \text{ (K km s}^{-1}\text{)} = 6 \times 10^{15} \int F_\nu dv \text{ (erg cm}^{-2} \text{ s}^{-1}\text{)}$). The origin of the map is at the J2000 equatorial coordinates of α Cen B, i.e. RA = $14^{\text{h}} 39^{\text{m}} 35^{\text{s}}.06$ and Dec = $-60^\circ 50' 15''.1$, and read-out positions are marked by crosses. At the time of observation (16 August 2012), the star is located at the centre of the white ring. The bright feature south of the map centre is also prominent in the continuum observations longward of 100 μm (cf. Fig. 2) and is the dominating source at 870 μm (Fig. 5).

For illustrative purposes, we place the object at a distance of 10 pc. Several ring temperatures were tested, and dust fluxes were adjusted to match the stellar RJ-SED. The modified black body of the dust was then adjusted to coincide with the difference in flux (i.e. stellar black body minus measured flux) at 160 μm and to a temperature that corresponds to the maximum of this flux difference.

This way of compensating for the T_{min} -effect resulted in a dust temperature $T_{\text{dust}} = 53 \text{ K}$ at the modified black body radius of 34 AU and a formal fractional luminosity $f_d = (2.2^{+1.2}_{-1.5}) \times 10^{-7}$, almost one order of magnitude below the detection limit of *Herschel*-PACS at 100 μm ($f_d \sim 10^{-6}$; see e.g. Fig. 1 of Eiroa et al. 2013) and comparable to what is estimated for the solar system Edgeworth-Kuiper belt ($\sim 10^{-7}$, Vitense et al. 2012). This fit is shown at the bottom of Fig. 8 where it is compared to the stellar SED and the difference between the black body and the

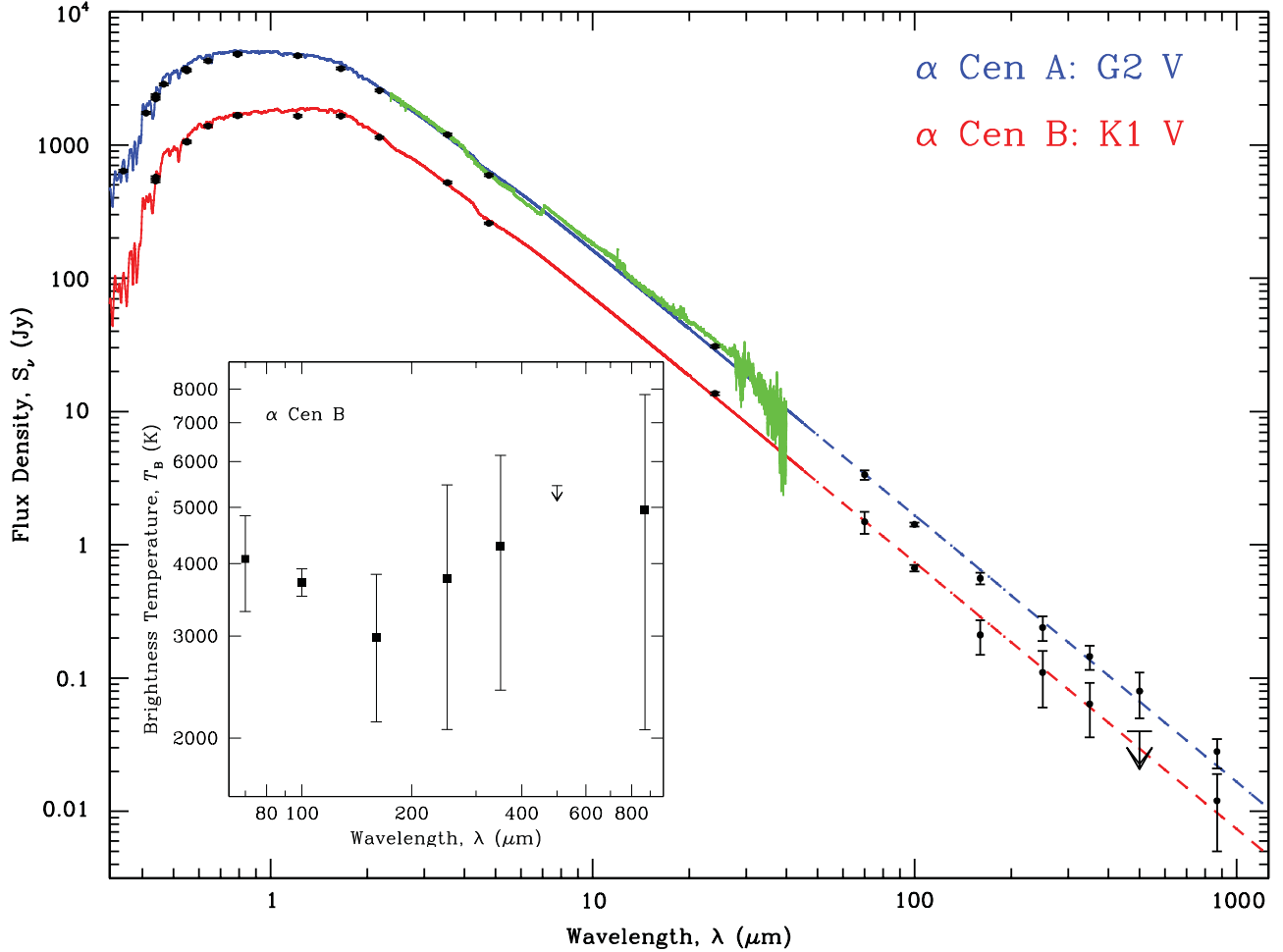


Fig. 7. SEDs of the binary α Cen AB. The model photospheres for the individual stars are shown by the blue and red lines. The PHOENIX model computations extend to about $45\ \mu\text{m}$ (solid lines). At longer wavelengths, these correspond to extrapolations using the proper $B_\nu(T_{\text{eff}})$ (dashes). Photometric data points are shown for comparison, with the upper limit being 3σ (Table 2). The green curve shows an ISO-SWS low-resolution observation, viz. TDT 60702006 (PI Waelkens; see also [Decin et al. 2003](#)). The *inset* displays the SED of the secondary α Cen B in the FIR/submm spectral region.

temperature minimum fit, whereas the upper panel shows the observed data points, the adopted run of the T_{min} -dip and that of the stellar RJ-SED.

Based on simple arguments, this dust temperature also provides a first-order estimate of the dust mass emitting at these wavelengths (cf. [Hildebrand 1983](#)), viz.

$$M_{\text{dust}} \sim \frac{\left[1 - \frac{S_{\text{min}}(\nu)}{S_{\text{model}}(\nu)}\right] S_{\text{model}}(\nu) D^2}{\kappa_{\text{ext}}(\nu) B(\nu, T_{\text{dust}})}. \quad (2)$$

For an α Cen-like star not showing the T_{min} effect, i.e. where the observed $S_{\text{obs, min}}(\nu) = S_{\text{model}}(\nu)$ (hence $M_{\text{dust}} = 0$), this formula would give a “concealed” dust mass of the order of the solar Edgeworth-Kuiper Belt (see e.g. [Wyatt 2008](#)), i.e. $\lesssim 10^{-3} M_{\odot}$ for $\kappa_{150\mu\text{m}} \gtrsim 10\ \text{cm}^2\ \text{g}^{-1}$, depending on the largest size a_{max} , the compactness and the degree of ice coating of the grains. For the cases considered here, reasonable values are within a factor of about 2 to 5 (e.g. [Miyake & Nakagawa 1993](#); [Krügel & Siebenmorgen 1994](#); [Ossenkopf & Henning 1994](#)). In general, $\kappa_{\text{ext}}(\nu) = \kappa_{\text{sca}}(\nu) + \kappa_{\text{abs}}(\nu)$ is the frequency-dependent mass extinction coefficient. At long wavelengths, say $\lambda > 5\ \mu\text{m}$, the

scattering efficiency becomes negligible for the grains considered here, and κ_{ext} reduces to κ_{abs} (κ_ν henceforth).

In the FIR, i.e. for low frequencies, one customarily approximates the opacity by a power law, i.e. $\kappa_\nu = \kappa_0 (\nu/\nu_0)^\beta$ when $\nu \leq \nu_0$, and where $\lambda_0 = c/\nu_0 > 2\pi a$ is a fiducial wavelength in the Rayleigh-Jeans regime, e.g. $\lambda_0 = 250\ \mu\text{m}$ ([Hildebrand 1983](#)). For spherical Mie particles, the exponent of the frequency dependence of the emissivity β is in the interval 1 to 2 for most grain materials ([Emerson 1988](#)). For blackbody radiation, $\beta = 0$. For circumstellar dust, β -values around unity have commonly been found (e.g. [Krügel & Siebenmorgen 1994](#); [Beckwith et al. 2000](#); [Wyatt 2008](#)).

The rough estimate from Eq. (2) only refers to the $a \leq 1\ \text{mm}$ regime and will thus not account for larger bodies, in many cases dominating the mass budget of debris discs (as in the solar system). As is commonly done in debris-disc studies, we distinguish between the dust mass and the total disc mass. To retrieve the mass of the unseen larger objects, numerical collisional models or analytical laws can be used (e.g. [Thébaud & Augereau 2007](#); [Wyatt 2008](#); [Löhne et al. 2008](#); [Heng & Tremaine 2010a,b](#); [Gáspár et al. 2012](#)), but we focus here solely

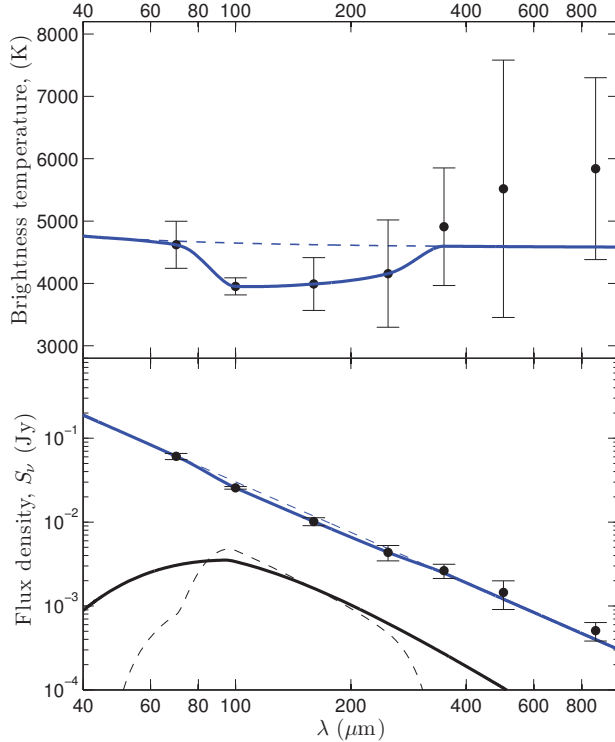


Fig. 8. *Top:* run of the brightness temperature of α Cen A, where the solid blue line is a fit through the data points around the temperature minimum, and the dashed blue line is the stellar blackbody extrapolation. The excess beyond $300\ \mu\text{m}$ is presumed to originate in higher chromospheric layers (e.g. De la Luz et al. 2013). *Bottom:* SED of α Cen A scaled to the distance of 10 pc. The dashed black curve is the difference between the black body extrapolation (dashed blue line) and the T_{min} -fit (solid blue line). The solid black curve is the emission of the fitted 53 K dust ring.

on the observable dust mass, which can be reasonably derived from infrared and submillimetre observations (Heng & Tremaine 2010a; Heng 2011). Even when obtained with an expression as simple as Eq. (2), these estimates are uncertain by at least a factor of several, because of uncertainties in the dust opacities.

From the dynamics of the binary system, we deduce (Appendix A) that a circumbinary disc is possible at a distance larger than 70–75 AU from the barycentre of the stars (see also Wiegert & Holman 1997; Jaime et al. 2012). Comparing the synthetic image of such a ring with an assumed outer radius of 105 AU in Fig. 3 with our observed continuum maps (Figs. 2 and 5), we find seemingly coherent structures at the proper distances of a face-on circumbinary ring. It is important to note that the circumbinary’s inclination may be unconstrained in contrast to the circumstellar discs that are dynamically limited to inclinations smaller than about 60° , (Wiegert & Holman 1997; see also Moutou et al. 2011 for a more general spin-orbit-inclination study). Also, Kennedy et al. (2012) report a circumbinary and circumpolar dust disc around 99 Herculis, which supports this possibility of non-coplanarity.

Regarding the possible detection of a circumbinary dust disc around α Cen AB, our single-epoch, multi-wavelength images would appear inconclusive. However, both proper motion and spectral line data obtained with APEX essentially rule out this scenario. If there is really a circumbinary disc or ring around α Centauri, it remained undetected by our observations.

Table 4. Properties of the α Centauri binary.

	α Cen A	α Cen B
Sp.type ^a	G2 V	K1 V
T_{eff} (K) ^b	5824 ± 24	5223 ± 62
L_{star} (L_{\odot}) ^b	$1.549^{+0.029}_{-0.028}$	$0.498^{+0.025}_{-0.024}$
M_{star} (M_{\odot}) ^{bc}	1.105 ± 0.007	0.934 ± 0.006
R_{star} (R_{\odot}) ^d	1.224 ± 0.003	0.863 ± 0.005
a_{crit} (AU) ^d	2.778 ± 1.476	2.522 ± 1.598
Common parameters		
Inclination to LOS, i ($^\circ$) ^c	79.20 ± 0.04	
Arg. of periaapsis, ω ($^\circ$) ^c	231.65 ± 0.08	
Long. of asc. node, Ω ($^\circ$) ^c	204.85 ± 0.08	
Period (yr) ^{bc}	79.91 ± 0.01	
Eccentricity ^c	0.5179 ± 0.0008	
Distance (pc) ^b	1.348 ± 0.035	
Age (yr) ^e	$(4.85 \pm 0.50) \times 10^9$	

References. ^(a) Kervella et al. (2003); ^(b) Torres et al. (2010); ^(c) Pourbaix et al. (2002); ^(d) Holman & Wiegert (1999); ^(e) Thévenin et al. (2002).

4.4. Mid Infrared: warm zodi-dust in asteroid-like belts around α Cen A and α Cen B

4.4.1. Stable orbits

The tentative excesses at $24\ \mu\text{m}$ may be due to warm dust. However, the binary nature of the α Cen system limits the existence of stable orbits to three possibilities. These are one large circumbinary disc with a certain inner radius and two circumstellar discs with maximum (or hereafter, critical) semi-major axes. These critical semi-major axes can be found using the semi-analytical expression of Holman & Wiegert (1999), viz.

$$a_{\text{crit}} = (c_1 + c_2 \mu + c_3 e + c_4 \mu e + c_5 e^2 + c_6 \mu e^2) a_{\text{AB}} \quad (3)$$

where e is the eccentricity of the binary orbit, $\mu = M_B/(M_A + M_B)$ i.e. the fractional mass of the stars, a_{AB} is the semi-major axis of the binary’s orbit, and the coefficients c_1 through c_6 (all with significant error bars) were computed by Holman & Wiegert (1999).

Using known parameters for α Cen (see Table 4), we can deduce that the circumstellar discs can not be larger than 2.78 ± 1.48 AU around α Cen A and 2.52 ± 1.60 AU around α Cen B, i.e. smaller than ~ 4 AU around either star (Table 4).

The putative Earth-mass planet, α Cen Bb (Dumusque et al. 2012) is small enough ($\sim 1.13 M_{\oplus}$) that its Hill radius is just 4×10^{-4} AU. Our model discs never reach closer to the star than 0.08 AU, and consequently, this planet was neglected in our disc modelling.

Owing to the large errors of the estimated a_{crit} , it was useful to test these limits with simple test-particle simulations of mass- and size-less particles. The resulting particle discs will also be used as a basis for radiative transfer simulations later. A steady state of these are shown in Fig. 9 where the accuracy of the Holman & Wiegert (1999) estimates is clear. Each simulation run was left for 10^3 orbital periods (i.e. $\sim 8 \times 10^4$ yr). The dynamics had earlier been examined also by others (e.g. Benest 1988; Wiegert & Holman 1997; Holman & Wiegert 1999; Lissauer et al. 2004; Thébault et al. 2009).

These size limits are reminiscent of the inner solar system, i.e. this opens the possibility of an asteroid belt analogue for each star that forms dust discs through the grinding of asteroids and comets. Temperature estimates for the solar system

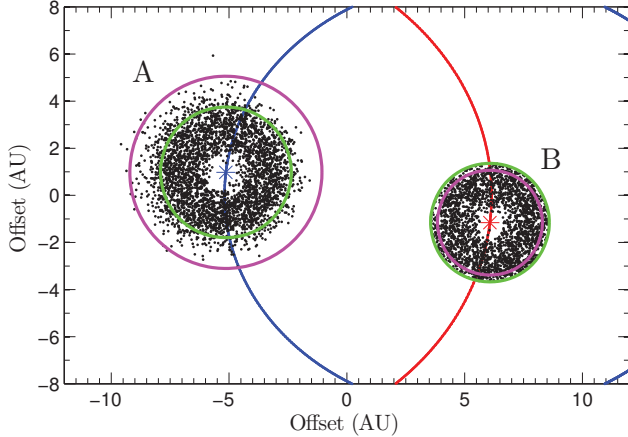


Fig. 9. Face-on circumstellar test-particle discs after $\sim 10^3$ periods shown with the stars close to periaapsis. α Cen A is colour-coded blue (the left star and its orbit), and α Cen B is colour-coded red (the right star and its orbit). The green circles represent a_{crit} around the stars and the magenta circles show estimates of their respective snow lines.

zodiacal cloud are around 270 K and that of the fractional luminosity is about 10^{-7} (Fixsen & Dwek 2002; Nesvorný et al. 2010; Roberge et al. 2012), i.e. f_d has a similar magnitude to the Edgeworth-Kuiper belt (Vitense et al. 2012).

4.4.2. Disc temperatures and snow lines

The *Spitzer* observations at $24\mu\text{m}$ (PSF $\geq 6''$, Table 2; see also Kennedy et al. 2012) would not fully resolve these dynamically allowed discs. Strict lower temperature limits are provided by black body radiation from the discs, i.e. $T_{\text{bb}} = \sqrt{R_{\text{star}}/(2R_{\text{bb}})} T_{\text{eff}} = 186$ K and 147 K, respectively, for α Cen A and B, where the ratio of absorption to emission efficiency of unity for a black body has been used (e.g. Liseau et al. 2008; Lestrade et al. 2012; Heng & Malik 2013).

The α Cen circumstellar discs are constrained to radii smaller than 4 AU and should be relatively warm. We need to know, therefore, the locations of the snow lines in order to understand the likelihood of the presence of icy grains on stable orbits around these stars.

The snow line can be defined to be the largest radial distance at which the sublimation time scale is larger than all other relevant time scales of the system (Artymowicz 1997). Our estimations are based on the equations and methods by Grigorieva et al. (2007) and by Lamy (1974). The sublimation time was compared with the orbital time as a lower limit and the system age (4.85×10^9 yr) as an upper limit. For the temperature-radius relation, we assumed blackbody emitters. This analysis resulted in sublimation temperatures between 154 K and 107 K for α Cen A, at the radial distances of 4.08 and 8.48 AU, respectively. Therefore, the snow line of α Cen A seems to be outside its dynamically stable region of 2.78 AU, which makes the presence of any icy disc grains not very likely (Fig. 9).

For α Cen B, sublimation temperatures were found to be between 157 K and 107 K, which corresponds to 2.23 and 4.81 AU, respectively. The lower bound is well inside the critical semi-major axis of 2.52 AU (see Fig. 9). Since this is based on an initial grain size of 1 mm (smaller sizes move the snow line outwards, while larger ones move it inwards), we can assume that the existence of a ring of larger icy grains and planetesimals is possible at the outer edge of the α Cen B disc. Such a ring could

supply the disc with icy grains. However, these cannot be expected to survive in such a warm environment for long. Thus we assume that the iceless opacities from Miyake & Nakagawa (1993) are sufficient in this case. Ossenkopf & Henning (1994) have computed opacity models for the growth of ice coatings on grains. This conglomeration generally results in higher opacities than for their bare initial state.

We use *dust* opacities that are based on the models presented by Miyake & Nakagawa (1993), but scaled by a gas-to-dust mass ratio of one hundred. For a “standard” size distribution (Lestrade et al. 2012), i.e. $n(a) \propto a^{-3.5}$, the work by Ossenkopf & Henning (1994) gave similar results (see also e.g. Krügel & Siebenmorgen 1994; Stognienko et al. 1995; Beckwith et al. 2000). These works had different scopes, addressing specifically coagulation processes, rather than destructive collisions. However, for bare grains these opacities may also be applicable to some extent for the dust in debris discs⁷.

In the following sections we present synthetic SEDs obtained with the radiative transfer program RADMC-3D (Dullemond 2012) to assess the disc configurations in more detail.

4.5. Energy balance, temperature, and density distributions

Isothermal blackbody emission from thin rings would not make a realistic scenario for the emission from dust belts or discs. In particular, we need to specify the run of temperature and density, which is obtained from the solution to the energy equation, balancing the radiative heating with the cooling by the optically thin radiation.

In this balance equation, the loss term expresses the flux density of this thermal dust emission from an ensemble of grains received at the Earth, viz.

$$S_{\text{dust}}(\nu) = \int \int 4\pi a^2 Q_{\nu, \text{abs}}(a) \frac{\pi B_{\nu}(T, r)}{4\pi D^2} n(a, r) da dr^3 \quad (4)$$

where $4\pi a^2 Q_{\nu, \text{abs}}(a)$ is the emissivity of the spherical grains with radius a , $Q_{\nu, \text{abs}}(a)$ is the absorption coefficient, $n(a, r)$ is the volume density of the grains at location r , πB_{ν} is the thermal emittance at the equilibrium temperature T at r , and D is the distance to the source (so that $4\pi D^2 \int S_{\text{dust}}(\nu) d\nu = L_{\text{dust}}$). The absorption coefficient $Q_{\nu, \text{abs}}$ is related to the dust opacity through $Q_{\nu, \text{abs}} = (4/3) \kappa_{\nu} \rho a$, where ρ is the grain mass density, $Q_{\nu, \text{abs}}$ is shown as function of wavelength for a variety of materials and compositions for two grain sizes (10 and 1000 μm) in Fig. 4 of Krivov et al. (2013). We discuss grain sizes in the next section.

4.5.1. Grain size distribution

It is often assumed that $n(a) \propto a^q$ describes the distribution in size of the grains (e.g. Miyake & Nakagawa 1993; Krügel & Siebenmorgen 1994; Ossenkopf & Henning 1994; Krivov et al. 2000). However, the shape, the existence, and magnitude of the power-law exponent q have been a matter of intense debate since Dohnanyi’s classic work on interplanetary particles in the solar system (Dohnanyi 1969). For a collision-dominated system at steady state, his result is summarised in a nutshell by the parameter $s = 11/6$, implying that $q = 2 - 3s = -3.5$ (see e.g. Dominik & Decin 2003; Wyatt 2008). This original work referred to the zodiacal cloud, but more recent estimates also for the much larger “grains”, i.e. Edgeworth-Kuiper belt objects

⁷ See also the homepage of B. Draine: <http://www.astro.princeton.edu/~draine/dust/dustmix.html>

(TNOs), by [Bernstein et al. \(2004\)](#) lead to a similar frequency spectrum for the diameters, $dn/dD \propto D^{-p}$ and $p = 4 \pm 0.5$, so that $q = -3 \pm 0.5$ (see also [Fraser & Kavelaars 2009](#)).

More recent works have been following the collisional time evolution of dusty debris discs using numerical statistical codes. They have found rather strong deviations from true power laws, showing wiggles and wavy forms due to resonances ([Krivov et al. 2006, 2013](#); [Thébaud & Augereau 2007](#); [Löhne et al. 2008](#); [Kral et al. 2013](#)). However, mean values of these oscillations may still be consistent with power-law exponents that are not too dissimilar from the steady state Dohnanyi-distribution. In fact, [Gáspár et al. \(2012\)](#) find, from a large number of simulations, that $q \sim -3.65$, i.e. slightly steeper than commonly assumed. Quoting [Miyake & Nakagawa \(1993\)](#), “ q will be large (~ -2.5) if the coagulation processes are dominant, whereas q will be small (~ -3.5) if the disruption processes are dominant”, one might infer that disruptive collisions would dominate in debris discs, as expected. To be consistent with the exploited opacities, but also for comparison reasons, we are using a Dohnanyi distribution, i.e. $n(a) \propto a^{-3.5}$ that we use henceforth. For simplicity, the distribution of particle sizes in the disc is assumed to be homogeneous⁸ since the grains are large enough to not be significantly affected by drag forces and radiation pressure.

In Eq. (4), the integral over a extends over the finite range a_{\min} to a_{\max} , where we adopt for a_{\max} the upper bound for the κ_{ν} -calculations, i.e. 1 mm. The smallest size, a_{\min} , is found for grains that are large enough not to be susceptible to the combined radiation pressure and stellar wind drag ([Strubbe & Chiang 2006](#); [Plavchan et al. 2009](#)), i.e.

$$a_{\min} > a_{\text{blow}} \approx \frac{3}{8\pi G M_{\text{star}} \rho_{\text{grain}}} \left[\frac{L_{\text{star}}}{c} + \dot{M}_{\text{star}} u_w \right], \quad (5)$$

where we have set the radiative and wind coupling coefficients to unity for this order of magnitude estimate. Inside the brackets are the radiative and the mechanical momentum rates (“forces”), respectively. The stellar mass loss rate of α Cen A is close to that of the Sun, i.e. $2 \times 10^{-14} M_{\odot} \text{ yr}^{-1}$, and also the average wind velocity is similar, viz. $v_w \sim 400 \text{ km s}^{-1}$ ([Wood et al. 2001, 2005](#))⁹. This implies that the second term in Eq. (5) is negligible and that $a_{\text{blow}} = 0.64 \mu\text{m}$ for the stellar parameters of Table 4 and a grain density of 2.5 g cm^{-3} (for α Cen B, the corresponding a -value is about three times lower). It has been shown that the lower cut-off size is smooth (e.g. [Wyatt et al. 2011](#); [Löhne et al. 2012](#), and references therein) and up to about six times the blow-out radius, i.e. $a_{\min} \sim 4 \mu\text{m}$.

In the next section, we calculate a number of numerical models for Eq. (4) by varying parameter values to get a feeling for how well (and uniquely) the observations can be reproduced. There were marginal excesses corresponding to 2.5σ at $24 \mu\text{m}$ for both α Cen A and α Cen B.

4.5.2. RADMC-3D exozodi-disc calculations

RADMC-3D is a Monte-Carlo radiative transfer code, written primarily for continuum radiation through dusty media in an

⁸ In general, grain sizes may not be homogeneously distributed throughout circumstellar discs. Smaller grains may be more abundant in the outer parts of the discs and may even reside in the dynamical unstable regions in a binary, owing to production through collisions and radiation pressure (e.g. [Thébaud et al. 2010](#)).

⁹ In this work the binary is not resolved into its components A and B, so that the quoted values refer to both of them. Although α Cen B is the more active star of the two, we simply assumed equal mass loss rates.

Table 5. Model parameters for RADMC-3D disc calculations.

Parameter (unit)	Value
Lower grain cut-off size, a_{\min} (μm)	4
Upper grain size limit, a_{\max} (μm)	1000
Power law exponent, $n(a) \propto a^{-q}$ (cm^{-3})	2.0, 2.5, 3.0, 3.5, 4.0
Power law exponent, $h(r) \propto r^{\beta}$ (AU)	0.0, 1.0
Power law exponent, $\Sigma(r) \propto r^{-\gamma}$ (g cm^{-2})	0, 1/2, 1, 3/2, 2, 6, 10
Grain mass density, ρ (g cm^{-3})	2.5
Vaporization temperature, T_{vap} (K)	750
Inner disc radius, R_{in} (AU)	$r(T_{\text{vap}})$
Outer disc radius, R_{out} (AU)	a_{crit}
Logarithmic dust mass (M_{\odot})	-7 through +4 by 0.1

arbitrary three-dimensional geometry (developed by [Dullemond 2012](#))¹⁰. It might seem an enormous “overkill” to use a radiative transfer program for the optically very thin discs discussed here, where the optical depth τ is comparable to the fractional luminosity f_{d} of the dust disc. However, RADMC-3D is a convenient and user-friendly means to solve the energy equation, calculate SEDs, and convolve the model-images with the appropriate response functions of the used equipment for the observations (e.g. transmission curves, PSFs or beams, etc.). Details regarding the computational procedure can be found in Appendix A and examined parameters are presented in Table 5.

The basic input to RADMC-3D is a stellar model atmosphere (we use 3D interpolations in the PHOENIX/GAIA grid, [Brott & Hauschildt 2005](#)), a grid with dust densities for each included dust species, and absorption and scattering coefficients at each wavelength and for each dust species. The inner disc radii are given by the dust vaporation temperature¹¹ of $\sim 750 \text{ K}$ and the outer radii determined by the binary dynamics. The discs have assumed height profiles $h \sim 0.05 r^{\beta}$, with $\beta = 0$ (or $\beta = 1$; e.g., [Wyatt 2008](#)).

Also based on the dynamical model parameters are the dust mass estimations for various power-law exponents of the surface density, $\Sigma \propto r^{-\gamma}$, where $\gamma \geq 0$. For reference, the solar minimum mass nebula (SMMN) has $\gamma = 1.5$ ([Hayashi 1981](#)). For the SMMN, at $r_0 = 1 \text{ AU}$, $\Sigma_0 \sim 2 \times 10^3 \text{ g cm}^{-2}$, whereas exo-planet systems may have slightly steeper laws and somewhat higher Σ_0 ([Kuchner 2004](#)).

Various grain size distributions were examined in accordance with Fig. 7 of [Miyake & Nakagawa \(1993\)](#), i.e. $-4 \leq q \leq -2$. The results of these computations are visualised in Fig. 10. There, we investigate whether any combination of parameters could be consistent with the observed data, i.e. the flux densities at 5, 24, and $70 \mu\text{m}$. For α Cen A, acceptable models would imply values of $f_{\text{d}} \sim 10^{-5}$ for its hypothetical zodi, where $q = -4$ to -3.5 . This would appear to agree with the result by [Gáspár et al. \(2012\)](#), i.e. $q = -3.65$.

However, no such model was found that would fit the data for α Cen B, as illustrated in the right-hand panel of Fig. 10. These models assume a flat Σ -distribution, i.e. $\gamma = 0$. To be compatible with the observations, models for $\gamma \neq 0$ would require very high values of γ (up to 10), making these “discs” more ring-like. However, best agreement was still achieved with $\gamma = 0$, when the model disc of α Cen B had less of an extent than the dynamically allowed size, i.e. $R_{\text{in}} = 0.1 \text{ AU}$ and $R_{\text{out}} = 0.5 \text{ AU}$. The temperature profile is given by $T(r) = 745 (r/0.05 \text{ AU})^{-0.55} \text{ K}$,

¹⁰ <http://www.ita.uni-heidelberg.de/~dullemond/software/radmc-3d/>

¹¹ This corresponds approximately to the low-density extrapolation of the data for olivine given by [Pollack et al. \(1994\)](#).

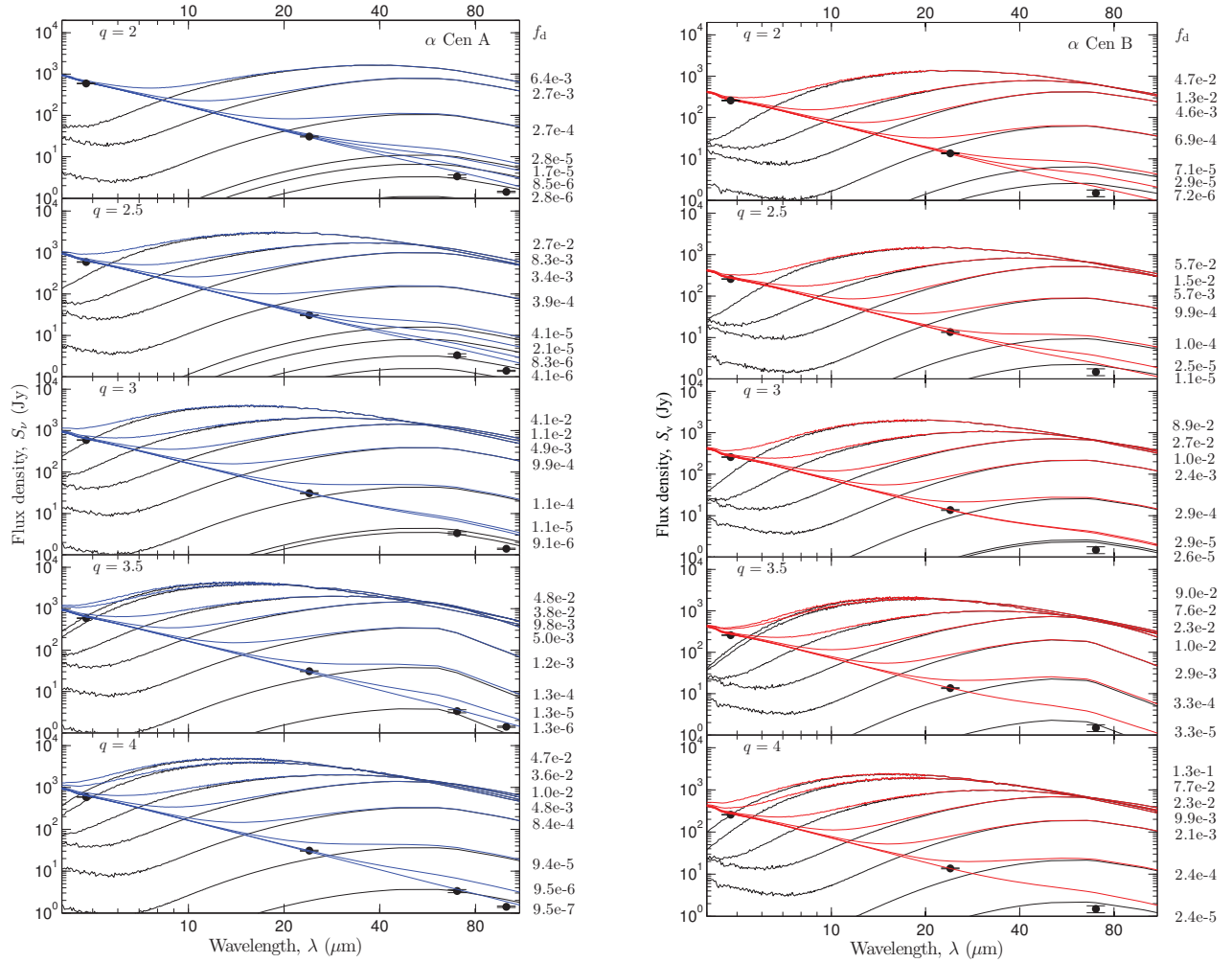


Fig. 10. *Left:* mid-infrared SEDs for α Cen A for different values of the power-law exponent q of the size distribution function, viz. $n(a) \propto a^{-q}$. Black curves depict dust SEDs, whereas blue curves display the total, i.e. $S_{\nu}^{\text{star}} + S_{\nu}^{\text{dust}}$. For each q , there are graphs for a selection of initial dust mass estimates and the fractional dust luminosity, $f_d = L_{\text{dust}}/L_{\text{star}}$, is shown next to each curve. The $100\mu\text{m}$ data were not part of the fitting procedure. *Right:* same as the left panel but for α Cen B and with the total emission shown in red.

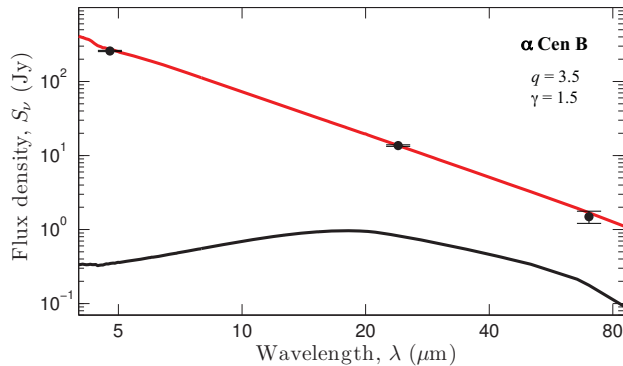


Fig. 11. Mid-infrared SED of α Cen B (star + dust, red curve) with data points. Assuming a “standard” disc model with $q = 3.5$ and $\gamma = 1.5$, the black curve shows the maximum emission from circumstellar dust that is consistent with the data.

and the dust-SED results in an $f_d = 3 \times 10^{-5}$ for a dust mass $m_d = 4 \times 10^{-6} M_{\odot}$ (3×10^{20} g, i.e. about $10 - 30 m_{\oplus}$) for grains with $a = 4\mu\text{m}$ to 1mm and with sizes according to a $q = -3.5$ power law (see Fig. 11).

For both α Cen A and B, these limiting values of f_d and m_d , respectively, would correspond to some 10^2 and 10 times those of the solar system zodiacal dust in $\lesssim 100\mu\text{m}$ size particles (Roberge et al. 2012; Fixsen & Dwek 2002; Nesvorný et al. 2010). Fixsen & Dwek (2002) estimate the total mass of the asteroid belt at about $0.03 M_{\odot}$ (2×10^{24} g). Heng & Tremaine (2010a,b) have calculated total disc masses for ages of about 3 Gyr. Their Fig. 7 would indicate that the mass of a “collision-limited” disc with a semi-major axis $\lesssim 4$ AU and detected at $24\mu\text{m}$ would amount to $\sim 0.1 M_{\odot}$. In both cases, these estimations refer effectively to discs around single stars, and it is not entirely clear to what degree this also applies to multiple systems.

5. Conclusions

Based on FIR and submm photometric imaging observations from space (*Herschel*) and the ground (APEX) of α Cen, the following main conclusions can briefly be summarised as

- Both binary components A and B were detected individually at $70\mu\text{m}$. At longer wavelengths, $100 - 870\mu\text{m}$, the pair was unresolved spatially during the time of observation, i.e. $8''4$ in 2007 to $5''7$ in 2011.

- At 100 and 160 μm , the solar twin α Cen A displays a temperature minimum in its SED, where the radiation originates at the bottom of its chromosphere. At longer wavelengths higher radiation temperatures are observed. This T_{min} -effect is also marginally observed for α Cen B.
- For solar-type stars not displaying the T_{min} -phenomenon, compensating for the “missing flux” by radiation from optically thin dust could account for fractional dust luminosities, $f_d \sim 2 \times 10^{-7}$, comparable to that of the solar system Edgeworth-Kuiper belt;
- Combining *Herschel* data with mid-infrared observations (*Spitzer*) indicates marginal (2.5σ) excess emission at 24 μm in the SEDs of both stars. If caused by circumstellar emission from dust discs, fractional luminosity and dust mass levels would be some 10 to 100 times those of the solar zodiacal cloud.

Acknowledgements. We thank the referee for the critical reading of the manuscript and the valuable suggestions that improved the quality of the paper. We are also grateful to H. Olofsson for granting his *Director’s Discretionary Time* to this project. We also wish to thank P. Bergman for his help with the APEX observations on such short notice and the swift reduction of the data. We appreciate the continued support of the Swedish National Space Board (SNSB) for our *Herschel* projects. The Swedish authors appreciate the continued support from the Swedish National Space Board (SNSB) for our *Herschel* projects. C. Eiroa, J. P. Marshall, and B. Montesinos are partially supported by Spanish grant AYA 2011/26202. A. Bayo was co-funded under the Marie Curie Actions of the European Commission (FP7-COFUND). S. Ertel thanks the French National Research Agency (ANR) for financial support through contract ANR-2010-BLAN-0505-01 (EXOZODI).

Appendix A: Orbital dynamics and disc modelling

The test particle simulations were done for two reasons: firstly, to assess the binary dynamics per se and, secondly, for the steady state results to be used as disc models for radiative transfer simulations.

The standard equation of motion for circumstellar dust grains (around a single star) sums up most of the physical processes a grain experiences and is written as (Robertson 1937; Stark & Kuchner 2008)

$$\begin{aligned} \mathbf{a}_n = & -\frac{GM_\star}{r_n^3} (1 - \mathcal{B}_n) \mathbf{r}_n \\ & - \frac{(1 + SW) \mathcal{B}_n}{c} \frac{GM_\star}{r_n^2} (\dot{r}_n \hat{\mathbf{r}} + \mathbf{v}_n) \\ & + \sum_i \frac{Gm_i}{|\mathbf{r}_i - \mathbf{r}_n|^3} (\mathbf{r}_i - \mathbf{r}_n) \end{aligned} \quad (\text{A.1})$$

for each test particle n . Here \mathcal{B}_n is the ratio between radiation pressure and gravitation exhibited on particle n , SW is the ratio between stellar-wind drag and Poynting-Robertson drag and is for the Sun about one third (~ 0.2 – 0.3 , Gustafson 1994), and m_i and \mathbf{r}_i are the mass and position of any planet in the system.

As hinted in Sect. 4.5.1, we consider grain sizes $\geq 4 \mu\text{m}$. This is more than six times the blow-out radius, and consequently, we only solve the classical restricted three-body-problem, i.e.

$$\mathbf{a}_n = -\frac{GM_A}{|\mathbf{r}_n - \mathbf{r}_A|^3} (\mathbf{r}_n - \mathbf{r}_A) - \frac{GM_B}{|\mathbf{r}_n - \mathbf{r}_B|^3} (\mathbf{r}_n - \mathbf{r}_B) \quad (\text{A.2})$$

for each test particle n . These simulations implemented a Runge-Kutta 4 integrator to solve the motions.

One particle disc was simulated at a time. The two circumstellar discs had identical initial conditions except for the central

star; i.e., they had 10^4 particles in discs with constant particle density and radii smaller than 5 AU. The circumbinary disc also had constant particle density but was 100 AU in radius, (This was varied, but we only show results from the disc with 100 AU radius.) The circumbinary disc’s outer radius is, in contrast to the circumstellar discs, not constrained by the employed dynamics. Therefore the outer edge seen in Fig. 3 is artificial.

All discs were left to run for 10^3 periods, i.e. $\sim 8 \times 10^4$ yr, which was found to be sufficient to achieve a steady state. That the disc had settled by that time was verified with much longer runs (e.g. $\sim 8 \times 10^5$ yr). At the inner edge of the circumstellar discs, the grid resolution was up to 0.047 AU. On the much larger scale of the circumbinary disc, time steps of 0.1 yr were sufficient.

Finally, particles that came either closer than 0.001 Hill radii to each star or farther out than 1000 AU from the barycentre were removed. These limits were arbitrarily set on the basis of previous tests. The number of particles remaining varied from run to run with e.g. 2496 as the lowest (α Cen B with initial disc radius of 5 AU) up to 6717 (again α Cen B but with initial disc radius of 0.2 AU). The α Cen A disc with initial radius of 5 AU had 3538 remaining particles.

To compute dust SEDs, the dust disc density grid was obtained directly from the steady state discs. These were converted to a grid of mass densities with a large number of initially guessed dust masses, m_{dust} . The proper temperature and density profiles yielded SEDs, which were compared to the data. The best fit was selected on the basis of its χ^2 -value.

References

- Artymowicz, P. 1997, *Ann. Rev. Earth Planet. Sci.*, 25, 175
- Avrett, E. H. 2003, in *Current Theoretical Models and Future High Resolution Solar Observations: Preparing for ATST*, eds. A. A. Pevtsov, & H. Uitenbroek, ASP Conf. Ser., 286, 419
- Ayres, T. R., Linsky, J. L., Rodgers, A. W., & Kurucz, R. L. 1976, *ApJ*, 210, 199
- Balog, Z., Müller, T., Nielbock, M., et al. 2013, *Experimental Astronomy*, DOI: 10.1007/s10686-013-9352-3
- Beck, C., Rezaei, R., & Puschmann, K. G. 2013, *A&A*, 556, A127
- Beckwith, S. V. W., Henning, T., & Nakagawa, Y. 2000, in *Protostars and Planets IV* (Tucson: Univ. of Arizona Press), 533
- Bendo, G. J., Griffin, M. J., Bock, J. J., et al. 2013, *MNRAS*, 433, 3062
- Benest, D. 1988, *A&A*, 206, 143
- Bernstein, G. M., Trilling, D. E., Allen, R. L., et al. 2004, *AJ*, 128, 1364
- Bessell, M. S. 1990, *PASP*, 102, 1181
- Bigot, L., Kervella, P., Thévenin, F., & Ségransan, D. 2006, *A&A*, 446, 635
- Brott, I., & Hauschildt, P. H. 2005, in *The Three-Dimensional Universe with Gaia*, eds. C. Turon, K. S. O’Flaherty, & M. A. C. Perryman, ESA SP, 576, 565
- Carlsson, M., & Stein, R. F. 1995, *ApJ*, 440, L29
- Dame, T. M., Hartmann, D., & Thaddeus, P. 2001, *ApJ*, 547, 792
- de la Cruz Rodríguez, J., De Pontieu, B., Carlsson, M., & Rouppe van der Voort, L. H. M. 2013, *ApJ*, 764, L11
- De la Luz, V., Raulin, J.-P., & Lara, A. 2013, *ApJ*, 762, 84
- Decin, L., Vandenbussche, B., Waelkens, K., et al. 2003, *A&A*, 400, 695
- Desidera, S., & Barbieri, M. 2007, *A&A*, 462, 345
- Dohnanyi, J. S. 1969, *J. Geophys. Res.*, 74, 2531
- Dominik, C., & Decin, G. 2003, *ApJ*, 598, 626
- Dullemond, C. P. 2012, *Astrophysics Source Code Library*, ascl: 1202.015
- Dumusque, X., Pepe, F., Lovis, C., et al. 2012, *Nature*, 491, 207
- Edvardsson, B. 2008, *Phys. Scr. T*, 133, 014011
- Eiroa, C., Marshall, J. P., Mora, A., et al. 2011, *A&A*, 536, L4
- Eiroa, C., Marshall, J. P., Mora, A., et al. 2013, *A&A*, 555, A11
- Emerson, J. P. 1988, in *NATO ASIC Proc. 241: Formation and Evolution of Low Mass Stars*, eds. A. K. Dupree & M. T. V. T. Lago, 21
- Endl, M., Kürster, M., Els, S., Hatzes, A. P., & Cochran, W. D. 2001, *A&A*, 374, 675
- Engels, D., Sherwood, W. A., Wamsteker, W., & Schultz, G. V. 1981, *A&AS*, 45, 5
- Fixsen, D. J., & Dwek, E. 2002, *ApJ*, 578, 1009
- Fraser, W. C., & Kavelaars, J. J. 2009, *AJ*, 137, 72

- Gáspár, A., Psaltis, D., Rieke, G. H., & Özel, F. 2012, *ApJ*, 754, 74
- Griffin, M. J., Abergel, A., Abreu, A., et al. 2010, *A&A*, 518, L3
- Grigorieva, A., Thébault, P., Artymowicz, P., & Brandeker, A. 2007, *A&A*, 475, 755
- Guedes, J. M., Rivera, E. J., Davis, E., et al. 2008, *ApJ*, 679, 1582
- Gustafson, B. A. S. 1994, *Ann. Rev. Earth Planet. Sci.*, 22, 553
- Gustafsson, B., Edvardsson, B., Eriksson, K., et al. 2008, *A&A*, 486, 951
- Hatzes, A. P. 2013, *ApJ*, 770, 133
- Hayashi, C. 1981, *Prog. Theor. Phys. Suppl.*, 70, 35
- Heng, K. 2011, *MNRAS*, 415, 3365
- Heng, K., & Malik, M. 2013, *MNRAS*, 432, 2562
- Heng, K., & Tremaine, S. 2010a, *MNRAS*, 405, 701
- Heng, K., & Tremaine, S. 2010b, *MNRAS*, 401, 867
- Hildebrand, R. H. 1983, *QJRAS*, 24, 267
- Holman, M. J., & Wiegert, P. A. 1999, *AJ*, 117, 621
- Jaime, L. G., Pichardo, B., & Aguilar, L. 2012, *MNRAS*, 427, 2723
- Kennedy, G. M., Wyatt, M. C., Sibthorpe, B., et al. 2012, *MNRAS*, 421, 2264
- Kervella, P., Thévenin, F., Ségransan, D., et al. 2003, *A&A*, 404, 1087
- Kral, Q., Thébault, P., & Charnoz, S. 2013, *A&A*, 558, A121
- Krivov, A. V., Mann, I., & Krivova, N. A. 2000, *A&A*, 362, 1127
- Krivov, A. V., Löhne, T., & Sremčević, M. 2006, *A&A*, 455, 509
- Krivov, A. V., Eiroa, C., Löhne, T., et al. 2013, *ApJ*, 772, 32
- Krügel, E., & Siebenmorgen, R. 1994, *A&A*, 288, 929
- Kuchner, M. J. 2004, *ApJ*, 612, 1147
- Lamy, P. L. 1974, *A&A*, 35, 197
- Leenaarts, J., Carlsson, M., Hansteen, V., & Gudiksen, B. V. 2011, *A&A*, 530, A124
- Lestrade, J.-F., Matthews, B. C., Sibthorpe, B., et al. 2012, *A&A*, 548, A86
- Liseau, R., Risacher, C., Brandeker, A., et al. 2008, *A&A*, 480, L47
- Liseau, R., Montesinos, B., Olofsson, G., et al. 2013, *A&A*, 549, L7
- Lissauer, J. J., Quintana, E. V., Chambers, J. E., Duncan, M. J., & Adams, F. C. 2004, in *Rev. Mex. Astron. Astrofis. Conf. Ser.* 22, eds. G. Garcia-Segura, G. Tenorio-Tagle, J. Franco, & H. W. Yorke, 99
- Löhne, T., Krivov, A. V., & Rodmann, J. 2008, *ApJ*, 673, 1123
- Löhne, T., Augereau, J.-C., Ertel, S., et al. 2012, *A&A*, 537, A110
- Maldonado, J., Eiroa, C., Villaver, E., Montesinos, B., & Mora, A. 2012, *A&A*, 541, A40
- Marshall, J. P., Moro-Martín, A., Eiroa, C., et al. 2014, *A&A*, accepted
- Miyake, K., & Nakagawa, Y. 1993, *Icarus*, 106, 20
- Moutou, C., Díaz, R. F., Udry, S., et al. 2011, *A&A*, 533, A113
- Nesvorný, D., Jenniskens, P., Levison, H. F., et al. 2010, *ApJ*, 713, 816
- Ossenkopf, V., & Henning, T. 1994, *A&A*, 291, 943
- Paardekooper, S.-J., & Leinhardt, Z. M. 2010, *MNRAS*, 403, L64
- Pagano, I., Linsky, J. L., Valenti, J., & Duncan, D. K. 2004, *A&A*, 415, 331
- Pilbratt, G. L., Riedinger, J. R., Passvogel, T., et al. 2010, *A&A*, 518, L1
- Playchan, P., Werner, M. W., Chen, C. H., et al. 2009, *ApJ*, 698, 1068
- Poglitsch, A., Waelkens, C., Geis, N., et al. 2010, *A&A*, 518, L2
- Pollack, J. B., Hollenbach, D., Beckwith, S., et al. 1994, *ApJ*, 421, 615
- Porto de Mello, G. F., Lyra, W., & Keller, G. R. 2008, *A&A*, 488, 653
- Pourbaix, D., Nidever, D., McCarthy, C., et al. 2002, *A&A*, 386, 280
- Roberge, A., Chen, C. H., Millan-Gabet, R., et al. 2012, *PASP*, 124, 799
- Robertson, H. P. 1937, *MNRAS*, 97, 423
- Roell, T., Neuhäuser, R., Seifahrt, A., & Mugrauer, M. 2012, *A&A*, 542, A92
- Shannon, A., & Wu, Y. 2011, *ApJ*, 739, 36
- Siringo, G., Kreysa, E., Kovács, A., et al. 2009, *A&A*, 497, 945
- Söderhjelm, S. 1999, *A&A*, 341, 121
- Stark, C. C., & Kuchner, M. J. 2008, *ApJ*, 686, 637
- Stognienko, R., Henning, T., & Ossenkopf, V. 1995, *A&A*, 296, 797
- Strubbe, L. E., & Chiang, E. I. 2006, *ApJ*, 648, 652
- Teplitz, V. L., Stern, S. A., Anderson, J. D., et al. 1999, *ApJ*, 516, 425
- Thébaud, P. 2011, *Celest. Mech. Dyn. Astron.*, 111, 29
- Thébaud, P., & Augereau, J.-C. 2007, *A&A*, 472, 169
- Thébaud, P., Marzari, F., & Scholl, H. 2009, *MNRAS*, 393, L21
- Thébaud, P., Marzari, F., & Augereau, J.-C. 2010, *A&A*, 524, A13
- Thévenin, F., Provost, J., Morel, P., et al. 2002, *A&A*, 392, L9
- Torres, G., Andersen, J., & Giménez, A. 2010, *A&ARv*, 18, 67
- Vitense, C., Krivov, A. V., Kobayashi, H., & Löhne, T. 2012, *A&A*, 540, A30
- Wiegert, P. A., & Holman, M. J. 1997, *AJ*, 113, 1445
- Wood, B. E., Linsky, J. L., Müller, H.-R., & Zank, G. P. 2001, *ApJ*, 547, L49
- Wood, B. E., Müller, H.-R., Zank, G. P., Linsky, J. L., & Redfield, S. 2005, *ApJ*, 628, L143
- Wyatt, M. C. 2008, *A&ARv*, 46, 339
- Wyatt, M. C., Clarke, C. J., & Booth, M. 2011, *Celest. Mech. Dyn. Astron.*, 111, 1
- Xie, J.-W., Zhou, J.-L., & Ge, J. 2010, *ApJ*, 708, 1566

- ¹ Department of Earth and Space Sciences, Chalmers University of Technology, Onsala Space Observatory, 439 92 Onsala, Sweden
e-mail: wiegert@chalmers.se
- ² Observatoire de Paris, Section de Meudon, 5 place Jules Janssen, Laboratoire d'études spatiales et d'instrumentation en astrophysique, 92195 Meudon Cedex, France
- ³ Department of Astronomy, Stockholm University, 106 91 Stockholm, Sweden
- ⁴ ESA – ESAC Gaia SOC, PO Box 78, 28691 Villanueva de la Cañada, Madrid, Spain
- ⁵ Jet Propulsion Laboratory, M/S 169-506, 4800 Oak Grove Drive, Pasadena CA 91109, USA
- ⁶ Departamento de Física Teórica, C-XI, Facultad de Ciencias, Universidad Autónoma de Madrid, Cantoblanco, 28049 Madrid, Spain
- ⁷ Departamento de Astrofísica, Centro de Astrobiología (CAB, CSIC-INTA), Apartado 78, 28691 Villanueva de la Cañada, Madrid, Spain
- ⁸ NASA Herschel Science Center, Infrared Processing and Analysis Center, MS 100-22, California Institute of Technology, Pasadena CA 91125, USA
- ⁹ Herschel Science Center – C11, European Space Agency (ESA), European Space Astronomy Centre (ESAC), PO Box 78, Villanueva de la Cañada, 28691 Madrid, Spain
- ¹⁰ UJF-Grenoble 1/CNRS-INSU, Institut de Planétologie et d'Astrophysique de Grenoble (IPAG) UMR 5274, 38041 Grenoble, France
- ¹¹ European Southern Observatory, Casilla 1900, Santiago 19, Chile
- ¹² Max Planck Institut für Astronomie, Königstuhl 17, 69117 Heidelberg, Germany
- ¹³ Astrophysics Science Division, NASA Goddard Space Flight Center, Greenbelt MD 20771, USA
- ¹⁴ Instituto Nacional de Astrofísica, Óptica y Electrónica, Luis Enrique Erro 1, Sta. Ma. Tonantzintla, Puebla, Mexico
- ¹⁵ Institute of planetary Research, German Aerospace Center, Rutherfordstrasse 2, 124 89 Berlin, Germany
- ¹⁶ Leiden Observatory, University of Leiden, PO Box 9513, 2300 RA Leiden, The Netherlands
- ¹⁷ Astrophysikalisches Institut und Universitätssternwarte, Friedrich-Schiller-Universität Jena, Schillergäßchen 2-3, 07745 Jena, Germany
- ¹⁸ Astrophysics Mission Division, Research and Scientific Support Department ESA, ESTEC, SRE-SA PO Box 299, Keplerlaan 1, 2200 AG Noordwijk, The Netherlands
- ¹⁹ NASA Goddard Space Flight Center, Exoplanets and Stellar Astrophysics Laboratory, Code 667, Greenbelt MD 20771, USA
- ²⁰ Dept. of Physics & Astronomy, The Open University, Walton Hall, Milton Keynes MK7 6AA, UK
- ²¹ Space Science & Technology Department, CCLRC Rutherford Appleton Laboratory, Chilton, Didcot OX11 0QX, UK
- ²² Institute for Theoretical Physics and Astrophysics, University of Kiel, Leibnizstraße 15, 24098 Kiel, Germany